





Article

Effects of the Concrete Strength and FRP Reinforcement Type on the Non-Linear Behavior of Concrete Deep Beams

Mostafa Kazemi ^{1,*}, Mohammad Daneshfar ², Yousef Zandi ^{3,*}, Alireza Sadighi Agdas ⁴, Negin Yousefieh ⁵, Leili Mohammadifar ⁶, Aida Rahmani ⁷, Mohammad Saberian ⁸, Amr Mamdouh ⁹, Mohamed Amine Khadimallah ^{10,11} and Jie Li ⁸

- ¹ GeMMe Building Materials, Urban and Environmental Engineering Division (UEE), University of Liege, 4000 Liège, Belgium
 - ² Department of Civil Engineering, Deylaman Institute of Higher Education, Lahijan 43131, Iran; moh4mmad.daneshfar@gmail.com
 - ³ Department of Civil Engineering, Tabriz Branch, Islamic Azad University, Tabriz 51579, Iran
 - ⁴ Ghateh Gostar Novin Company, Tabriz 51579, Iran; alireza.sadighi.agdas@gmail.com
 - ⁵ Department of Civil Engineering, University of Tehran, Tehran 14179, Iran; negin.yousefieh94@gmail.com
 - ⁶ Faculty of Architectural Engineering, Islamic Azad University, Kerman Branch, Kerman 1167, Iran; leilimohammadifar@gmail.com
 - ⁷ Centre for Infrastructure Engineering, Western Sydney University, Penrith, NSW 2751, Australia; aida.rahmani63@gmail.com
 - ⁸ School of Engineering, RMIT University, Melbourne, VIC 3000, Australia; mohammad.boroujeni@rmit.edu.au (M.S.); jie.li@rmit.edu.au (J.L.)
 - ⁹ Architectural Department, Faculty of Engineering and Technology, Future University in Egypt, New Cairo 11845, Egypt; amr.mamdouh@fue.edu.eg
 - ¹⁰ Civil Engineering Department, College of Engineering, Prince Sattam Bin Abdulaziz University, Al-Kharj 16273, Saudi Arabia; m.khadimallah@psau.edu.sa
 - ¹¹ Laboratory of Systems and Applied Mechanics, Polytechnic School of Tunisia, University of Carthage, Tunis 1054, Tunisia
- * Correspondence: mostafa.kazemi@uliege.be (M.K.); zandi@iaut.ac.ir (Y.Z.)



Citation: Kazemi, M.; Daneshfar, M.; Zandi, Y.; Sadighi Agdas, A.; Yousefieh, N.; Mohammadifar, L.; Rahmani, A.; Saberian, M.; Mamdouh, A.; Khadimallah, M.A.; et al. Effects of the Concrete Strength and FRP Reinforcement Type on the Non-Linear Behavior of Concrete Deep Beams. *Sustainability* **2022**, *14*, 4136. <https://doi.org/10.3390/su14074136>

Academic Editor: Hesam Kamyab

Received: 25 February 2022

Accepted: 23 March 2022

Published: 30 March 2022

Publisher's Note: MDPI stays neutral with regard to jurisdictional claims in published maps and institutional affiliations.



Copyright: © 2022 by the authors. Licensee MDPI, Basel, Switzerland. This article is an open access article distributed under the terms and conditions of the Creative Commons Attribution (CC BY) license (<https://creativecommons.org/licenses/by/4.0/>).

Abstract: To provide sustainable reinforced concrete deep beams, the replacement of steel rebars by FRP rebars with high-chemical resistance is proposed by researchers. However, the effects of the concrete strength, top and web longitudinal reinforcements, and types of FRP flexural rebars on the non-linear performance of concrete deep beams have rarely been evaluated. This study numerically assessed the effects of the top and web longitudinal reinforcements and concrete strength on the non-linear behaviour of GFRP- and CFRP-strengthened concrete deep beams with various shear span-to-overall depth (a/h) ratios. As per the results, the highest tensile stress was obtained for the steel reinforcement, and the tensile stress in the CFRP reinforcement was more than that of the GFRP reinforcement under the failure load. Meanwhile, the results of high- and normal-strength concrete deep beams with the web reinforcement (16.4%) were lower than those without the web reinforcement (22.3%). Therefore, the web reinforcement moderately compensated for the low strength of normal concrete and the absence of the top longitudinal rebar to reinforce concrete deep beams in carrying the ultimate load. Furthermore, the participation of the GFRP reinforcement with the high-strength concrete was more than that with the normal-strength concrete in carrying a higher amount of loading.

Keywords: FE analysis; non-linear behaviour; web longitudinal reinforcement; GFRP and CFRP rebars; concrete strength

1. Introduction

The application of deep-reinforced concrete beams in the construction sector has drawn the attention of many researchers and members of the construction industries, because this type of beam has been widely used to improve the performance of high-rise

buildings, offshore structures, shear walls, and bridges due to its high shear resistance [1–3]. However, it may cause steel reinforcement rebars to corrode if the beam is exposed to harsh environmental conditions. Considering the use of sustainable materials for the construction sector has been proposed by researchers [4–27], and the replacement of steel rebars with FRP rebars has been taken into account as a viable solution to enhance the corrosion resistance of deep-reinforced concrete beams [4,5,28–33].

Different types of FRP rebars, such as glass fibre reinforced polymer (GFRP) and carbon fibre reinforced polymer (CFRP) rebars, have been used for concrete beam reinforcement. GFRP and CFRP rebars as applicable FRP composite materials are known for their high chemical resistance and low density [34–37]. However, the modulus of elasticity and bond performance of embedded FRP rebars in concrete materials are not as good as those of steel rebars. The bond quality of FRP rebar appeared to be higher with high-strength concrete materials than normal-strength concrete materials [38,39]. Therefore, the bond quality of FRP rebars can be somewhat enhanced by using high-strength concrete materials to improve the load-bearing resistance of structural members such as deep-reinforced concrete beams [39–41].

The shear performance of concrete deep beams strengthened with bottom GFRP rebars was assessed by Abed et al. [1]. They reported that the mid-span displacement of GFRP-strengthened concrete deep beams was more than that of the steel-strengthened concrete deep beams owing to the minor modulus of elasticity of GFRP rebars compared to the steel rebars. Meanwhile, an extensive diagonal cracking and high mid-span deflection appeared for GFRP-strengthened concrete deep beams when increasing the shear span-to-overall depth (a/h) ratio. In addition, the dowel action of GFRP rebars was lower than that of the steel rebars due to the lower tensile strength of GFRP rebars than that of the steel rebars. Farghaly and Benmokrane [42] evaluated the shear performance of concrete deep beams strengthened with GFRP and CFRP rebars, and without web reinforcements. As per the results, the reinforced concrete deep beams' ultimate load-bearing resistance was influenced by the reinforcement ratio. Furthermore, the failure modes of all concrete beams were brittle, thereby a diagonal shear failure was followed by concrete crushing. Another study by Andermatt and Lubell [43] assessed the flexural resistance of concrete deep beams strengthened with a bottom GFRP rebar. They demonstrated that the shear strength of strengthened concrete deep beams increased by decreasing the a/h ratio. A numerical study by Chen et al. [44] on concrete deep beams strengthened with FRP rebars showed that the aggregate interlock action was a key mechanism, causing the reinforcing stiffness to influence the shear strength. Mohamed et al. [45] assessed the behavior of continuous concrete deep beams strengthened with GFRP rebars. As per the results, the load capacity of the beams was dramatically reduced as the a/h ratio increased due to a drop in the strut's angle of inclination. Zinkaah and Ashour [46] predicted the load capacity of continuous concrete deep beams strengthened with GFRP rebars. They showed that the expected loads of the specimens strengthened with GFRP rebars were overestimated by the upper bound analysis. Thomas and Ramadass [47] evaluated the deflection response of concrete deep beams strengthened with GFRP. According to the results, with increasing beam depth the normalized shear stress decreased. Moreover, in deep beams, the vertical deflection at the loading point was identical to that at mid-span.

The effect of web longitudinal GFRP rebars on the concrete deep beams' flexural performance was evaluated by researchers. Concerning this, Mohamed et al. [48] assessed the effect of web reinforcement on the flexural behaviour of concrete deep beams. They showed that the crack width could be controlled by the web reinforcement. However, the ultimate load-bearing capacity was not affected by the presence of web longitudinal FRP rebars, while the a/h ratio of the concrete deep beam affected the participation of web steel reinforcement in the shear-carrying capacity as reported by Ashour [49]. Recently, Zinkaah et al. [50] evaluated the performance of concrete deep beams strengthened with top, bottom, and web GFRP rebars. They found that the failure mode of a unreinforced concrete deep beam was nearly the same as that of that reinforced with web GFRP re-

bars, where both of them failed due to the generation of a diagonal crack between the loading plate and the interior support plate. Previous studies have mainly focused on experimentally evaluating the flexural behaviour of concrete deep beams reinforced with GFRP bars. However, the influence of the concrete strength on the stress distribution in concrete deep beams reinforced with GFRP and CFRP has rarely been assessed. In addition, few studies have been conducted to assess the effect of top and web longitudinal reinforcements and FRP flexural rebars types on the non-linear performance of concrete deep beams. Moreover, analysis is required of the influence of concrete deep beams' depth on their flexural performance when they are reinforced with different types of FRP rebars. Furthermore, there is a demand to precisely understand the effect of a/h ratio on the stress distribution in the deep beams. Therefore, this study numerically assessed the non-linear behaviour of GFRP and CFRP-strengthened concrete deep beams with different a/h ratios under applied loads of first flexural and diagonal cracks and failure load. Meanwhile, the effect of web longitudinal GFRP rebars on the concrete deep beams' stress distribution was assessed. Thereafter, the flexural resistance of concrete deep beams with the absence of top longitudinal reinforcement was analyzed. Finally, a comparison was performed between the GFRP reinforced high- and normal-strength concrete deep beams.

2. Methodology

Figure 1 shows the flowchart of the research methodology in this study. First, the numerical models' outputs were validated with the concrete deep beams' results given by Zinkaah et al. [50]. Next, the effect of deep beams' height, GFRP rebars, and a/h ratio on the non-linear performance of numerical models was assessed. Then, the influence of steel, GFRP, and CFRP longitudinal reinforcements and concrete strength on the stress distribution in concrete deep beam models was evaluated. The details of numerical models and material properties are presented in the following sections:

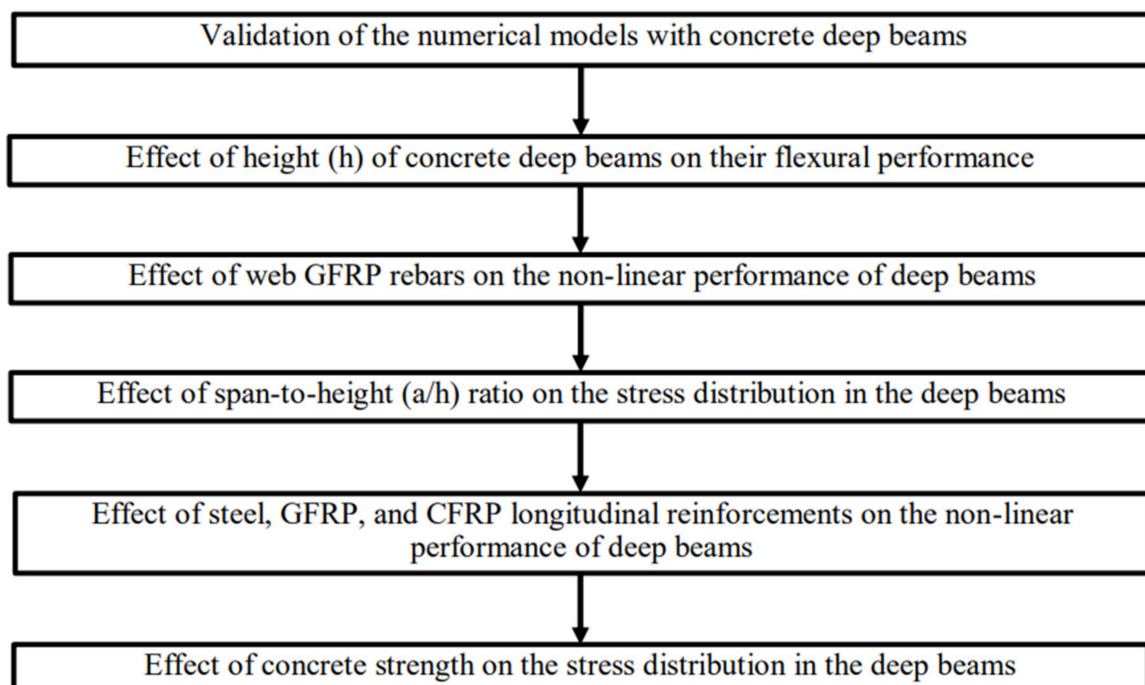


Figure 1. Flowchart of research methodology.

2.1. Details of Numerical Models

In this study, fifteen reinforced concrete deep beams were modeled. The experimental outputs specified by Zinkaah et al. [50] were employed to validate the numerical models with reference numbers of 1–10, as presented in Table 1. Nine numerical models with

different depths and a/h ratios were reinforced with and without GFRP rebars (reference numbers of 1–9). The model with a reference number of 10 was reinforced with steel rebar. After verifying the aforementioned numerical models, the mechanical properties of top and bottom GFRP rebars were replaced with CFRP rebars in the numerical model with the reference number of 11 (C1-600-N); then the effects of GFRP, steel, and CFRP rebars on the reinforced concrete deep beams' flexural performance were compared to each other. To obtain the number of top and bottom CFRP rebars, the axial stiffness of the GFRP rebar ($E_{gf}A_{gf}$) was equated to that of the CFRP rebar ($E_{cf}A_{cf}$), where E_{gf} and A_{gf} are the modulus of elasticity and the area of GFRP rebar, and E_{cf} and A_{cf} are the modulus of elasticity and the area of CFRP rebar.

Table 1. Details of the reinforced concrete deep beams.

No.	Specimen	h^a (mm)	d^b (mm)	a^c (mm)	a/h	a/d	L^d (mm)	l_d^e (mm)	b^f (mm)	Concrete Strength (MPa)	Type of Top and Bottom Reinforcements
1	G ^g 1 – 300 – N ^h	300	260	300	1	1.15	600	400	175	54	GFRP
2	G1 – 300 – W ⁱ	300	260	300	1	1.15	600	400	175	54	GFRP
3	G1.7-300-N	300	260	510	1.7	1.15	1020	400	175	54	GFRP
4	G1.7-300-W	300	260	510	1.7	1.96	1020	400	175	54	GFRP
5	G1-600-N	600	520	600	1	1.15	1200	400	175	54	GFRP
6	G1-600-W	600	520	600	1	1.15	1200	400	175	54	GFRP
7	G1.7-600-W	600	520	1020	1.7	1.96	2040	400	175	54	GFRP
8	G1-800-N	800	695	800	1	1.15	1600	400	175	54	GFRP
9	G1-800-W	800	695	800	1	1.15	1600	400	175	54	GFRP
10	S ^j 1-600-N	600	554	600	1	1.08	1200	150	175	54	Steel
11	C ^k 1-600-N	600	520	600	1	1.15	1200	400	175	54	CFRP
12	G1 – 600 – N – AT ^l	600	520	600	1	1.15	1200	400	175	54	GFRP
13	G1-600-W-AT	600	520	600	1	1.15	1200	400	175	54	GFRP
14	G1-600-N-30	600	520	600	1	1.15	1200	400	175	30	GFRP
15	G1-600-W-30	600	520	600	1	1.15	1200	400	175	30	GFRP

^a Beam depth; ^b Effective depth of the concrete section; ^c Shear span; ^d Centre to centre of the beam span; ^e Development length of the longitudinal reinforcement; ^f Beamwidth; ^g Deep beam reinforced with GFRP top and bottom rebars; ^h Deep beam with no web reinforcement; ⁱ Deep beam with web reinforcement; ^j Deep beam with the absence of top reinforcement; ^k Deep beam reinforced with CFRP top and bottom rebars; ^l Specimen with FRP rebars.

On the other hand, the top reinforcements were omitted from two verified numerical models to analyze the nonlinear performance of concrete deep beams with and without top reinforcements (G1-600-N-AT and G1-600-W-AT). The compressive strength of numerical models with reference numbers 1–13 was equal to 54 MPa. To assess the influence of concrete strength on the results of this study, the compressive strength of 30 MPa was introduced to two other models (G1-600-N-30 and G1-600-W-30). Figure 2 shows the details of numerical models, similar to the experimental specimens cast and tested by Zinkaah et al. [50].

2.2. Features and Element Types of the Reinforced Concrete Deep Models

As per Figure 3, the strengthened concrete deep beams included stirrup, concrete deep beam, top, bottom, and web reinforcements, three rigid sections as exterior and interior support plates, and two other rigid sections as loading plates. The three-dimensional (3D) hexahedral element was employed for modeling of the concrete beams [51–55]. The truss element type of 3D deformable wire was used for modeling the reinforcements.

Figure 3 depicts the load-applying surfaces. The interface between loading plates and concrete components was assumed to be the constraint of the tie. The surface to surface contact was introduced to the concrete component and support plates' interface, in which no slip took place when points were in interaction. The displacement of exterior and

interior support plates was restricted to achieve reliable numerical models, likewise to that considered by Zinkaah et al. [50], to design the experimental specimens.

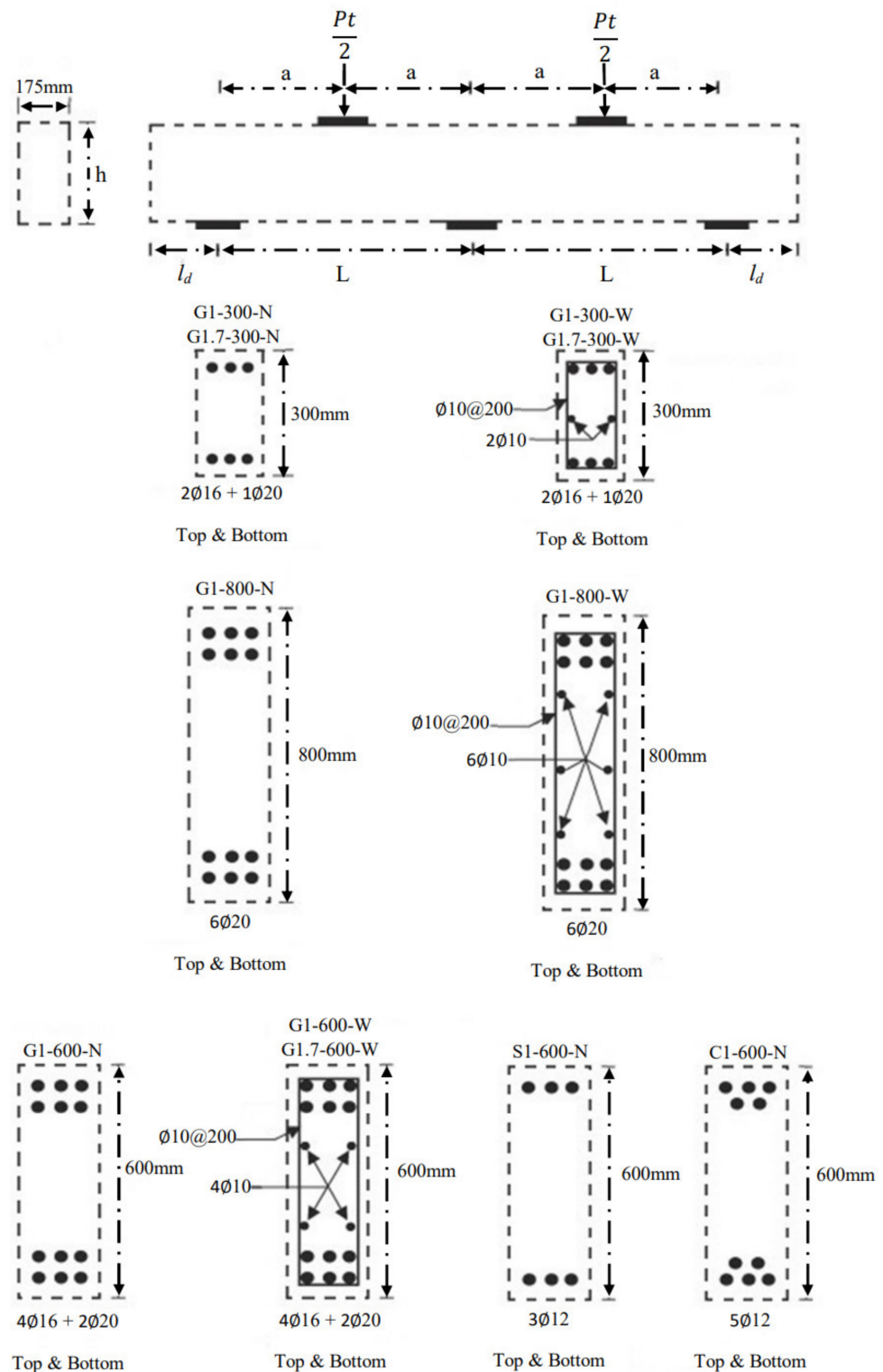


Figure 2. Details of deep beams reinforced with GFRP, CFRP, and steel reinforcements.

To validate the numerical models, approximate element sizes of 0.03, 0.03, 0.08, 0.035, 0.092, 0.03, 0.08, 0.1, 0.05, 0.092 m were assumed for G1-300-N, G1-300-W, G1.7-300-N, G1.7-300-W, G1-600-N, G1-600-W, G1.7-600-W, G1-800-N, G1-800-W, and S1-600-N, respec-

tively, along with the longitudinal reinforcements and whole beam length. The corresponding values for G1-600-N-AT and G1-600-W-AT were the same as those considered for G1-600-N and G1-600-W, respectively. The same values were assumed for G1-600-N-30 and G1-600-W-30, respectively. The approximate element size of C1-600-N was equal to that of G1-600-N.

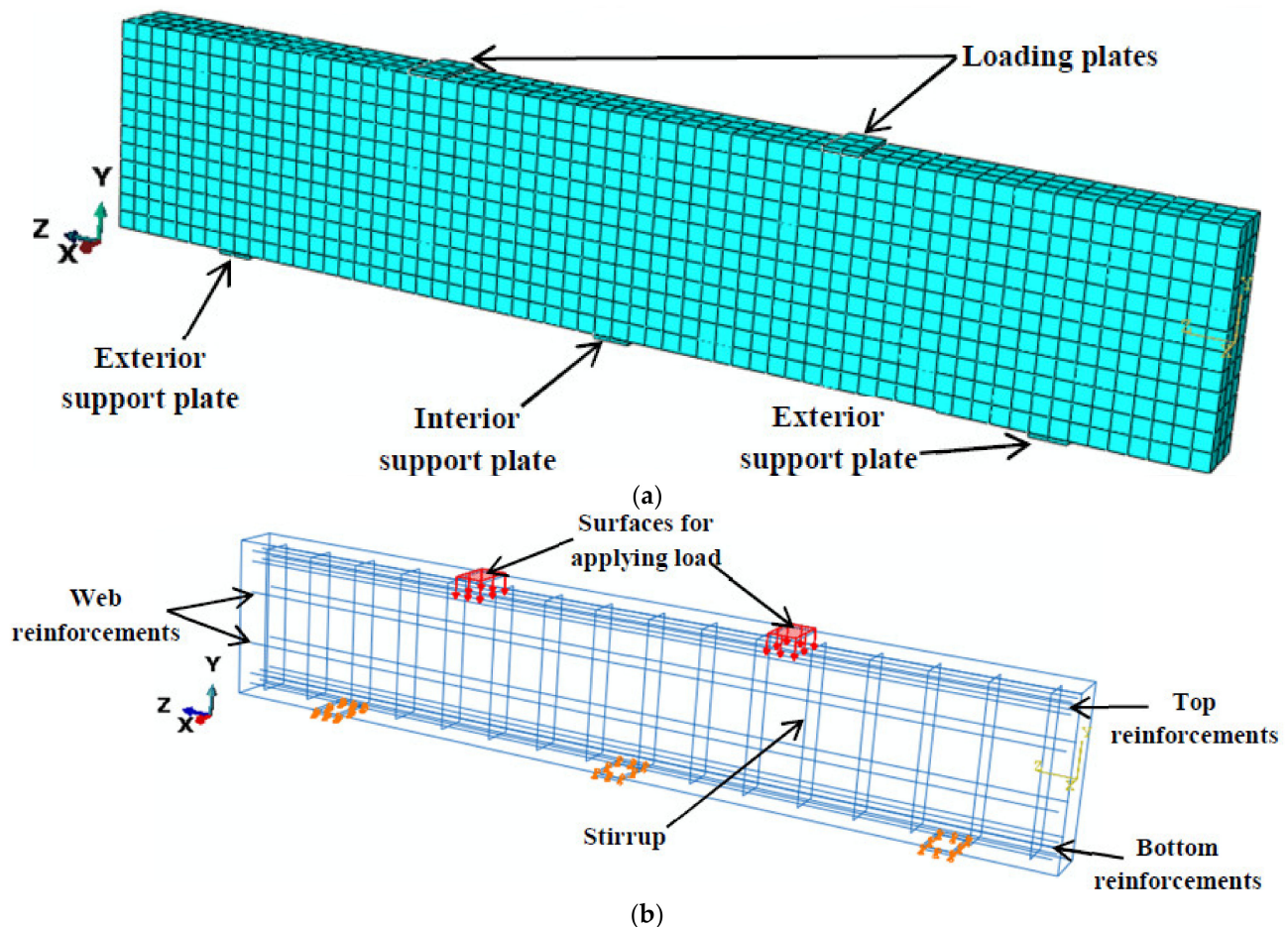


Figure 3. Finite element mesh (a); and components of G1-600-W model (b).

2.3. Material Properties

2.3.1. Reinforcements

As presented in Table 2, the mechanical characteristics of steel and GFRP rebars used for the numerical modeling were the same as those considered by Zinkaah et al. [50]. The corresponding properties for the CFRP rebar were assumed, based on the suggestions given by De Lorenzis et al. and Brozda et al. [56,57]. It is noteworthy that the GFRP rebar with a diameter of 10 mm was introduced to the stirrups in the numerical models. The diameter of the web longitudinal GFRP rebar was also equal to 10 mm. Meanwhile, the steel and CFRP rebar with a diameter of 12 mm and GFRP rebar with diameters of 16 and 20 mm were used for the top and bottom reinforcements, respectively. The Poisson ratio of all types of bars was assumed to be equal to 0.3.

2.3.2. Concrete

To simulate the concrete component's behaviour in compression and tension, the concrete damaged plasticity (CDP) crack model was employed as provided in ABAQUS

software (Figure 4). The stress equations against the strain of concrete at tension and compression are shown in Equations (1) and (2), respectively.

$$\sigma_t = (1 - d_t)E_0 (\varepsilon_t - \varepsilon_t^{pl}) \quad (1)$$

$$\sigma_c = (1 - d_c)E_0 (\varepsilon_c - \varepsilon_c^{pl}) \quad (2)$$

where compressive damage variable (DAMAGEC) is referred to as d_c and tensile damage variable (DAMAGET) is referred to as d_t . Also, E_0 is concrete Young's modulus, and ε_t^{pl} and ε_c^{pl} are equivalent plastic strains at tension and compression, respectively [58,59].

Table 2. Mechanical characteristics of steel, GFRP, and CFRP rebars.

Type of the Rebar	Diameter of Rebar, d_b , (mm)	Area of Flexural Rebar, A_f , (mm ²)	Yield Stress, f_y , (MPa)	Ultimate Stress (f_{tu}) (MPa)	Modulus of Elasticity, E_f , (GPa)	$A_f E_f$ (MN)	Poisson Ratio
Steel	12	98	548	650	200.8	19.7	0.3
GFRP	10	73	-	1100	62.6	4.6	0.3
	16	180	-	920	48.7	8.8	0.3
	20	278	-	760	43.5	12.1	0.3
CFRP	12	98	-	2300	130	12.7	0.3

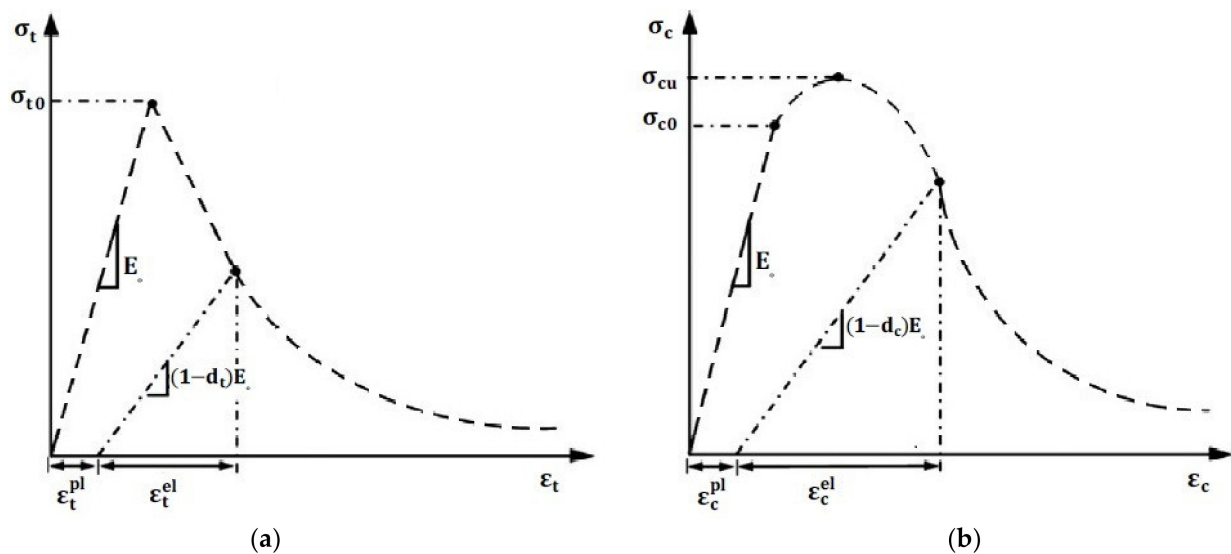


Figure 4. Proposed non-linear tensile (a) and compressive (b) behaviors of concrete components, employed in ABAQUS.

To develop the CDP model, it was mandatory to introduce some specific parameters to the ABAQUS software. The modification coefficient of the deviatoric plane (K_c) was considered to be 0.667 to keep the deviatoric cross-section's failure surface under control [60]. The initial biaxial compressive yield stress ratio to initial uniaxial compressive yield stress (σ_{b0}/σ_{c0}) was 1.16 [57]. As proposed by Michał and Andrzej [61], the dilation angle parameter (ψ) was assumed to be equal to 31 degrees to consider the concrete behavior under the compound stress. The flow potential eccentricity parameter (ϵ) was assumed to be 0.1, as recommended by researchers [51], to consider the ration between concrete tensile strength and compressive strength. A minimal value was also presented to the ABAQUS for the viscosity parameter (μ), as recommended by researchers [51,58].

3. Validation of Reinforced Concrete Deep Models

As depicted in Figure 5, the total load vs. mid-span deflection curves, drawn from numerical results, were compared with those of the experimental outputs specified by Zinkaah et al. [50]. In Figure 5, the mid-span deflection was obtained for each span, which was the vertical displacement of the concrete component between the interior support plate and one of the exterior support plates. As per the results, the gradients of curves for numerical models were nearly the same as those obtained from the experimental investigation. In addition, Figure 6 showed that the tensile damage variable (DAMAGET) of reinforced concrete deep models exhibited the evolution of a main internal diagonal crack between the interior support plate and one of the loading plates, similar to that which appeared in the experimental investigation performed by Zinkaah et al. [50].

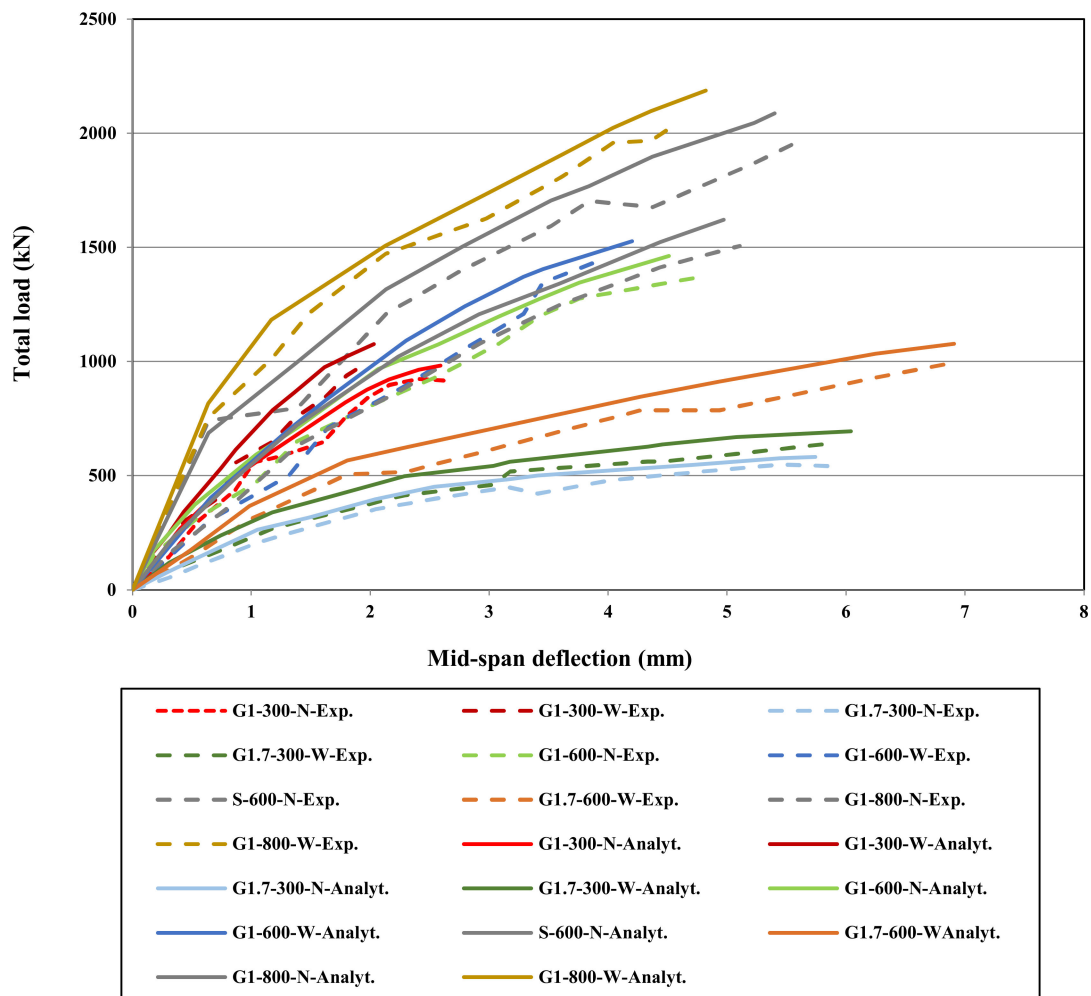


Figure 5. Plot of load vs. mid-span deflection for the deep beams.

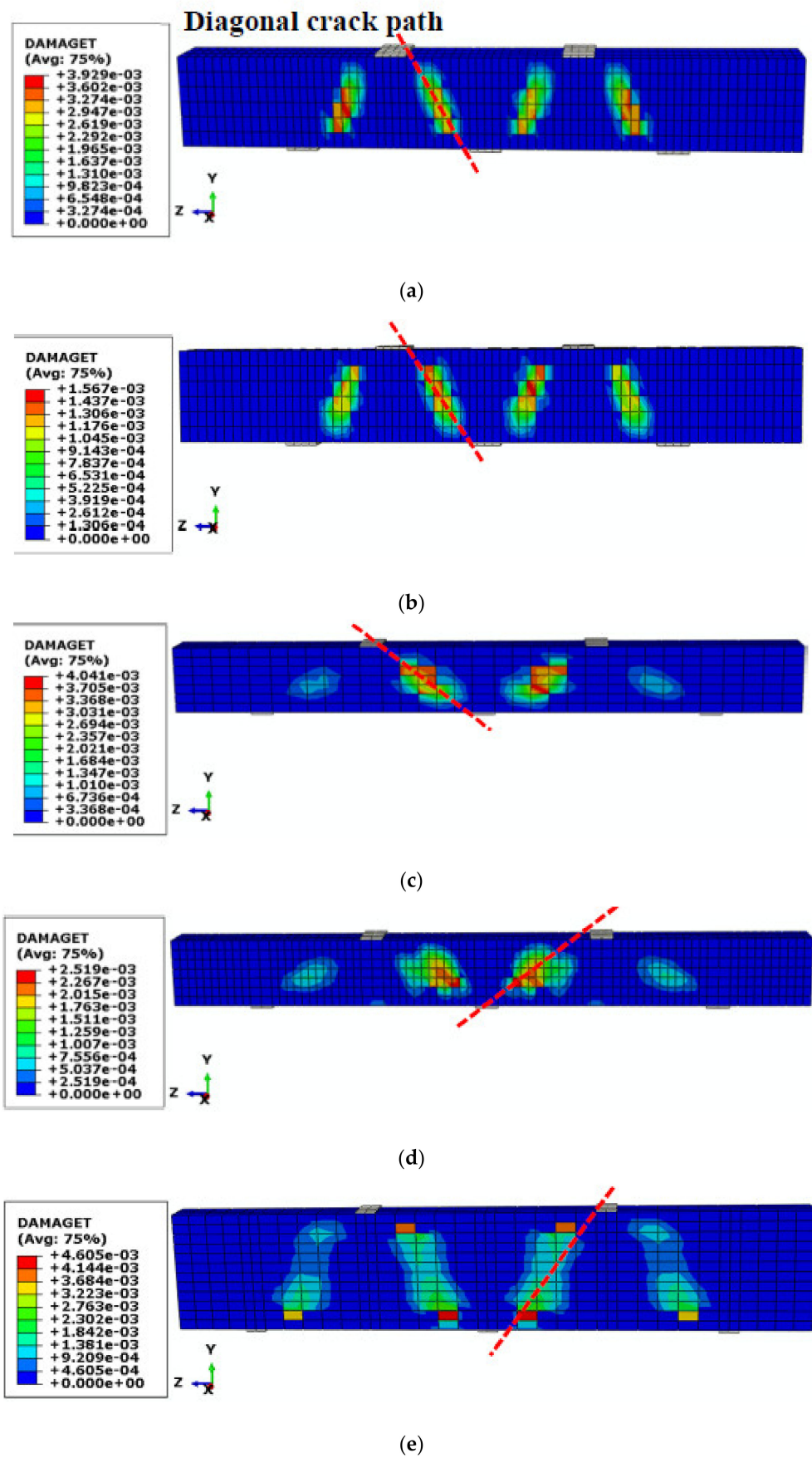
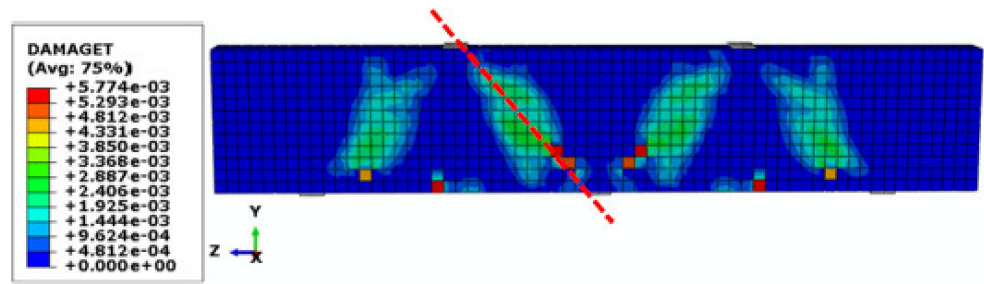
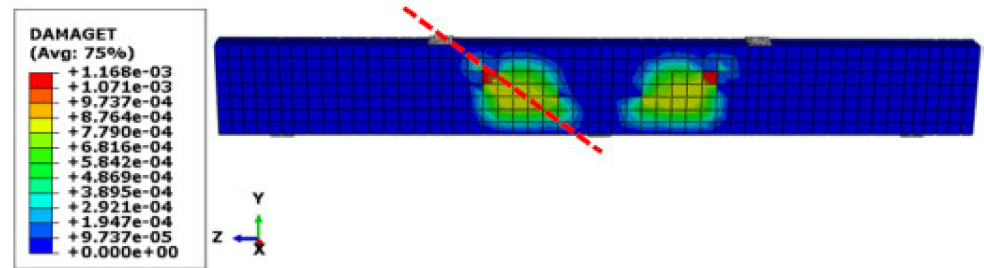


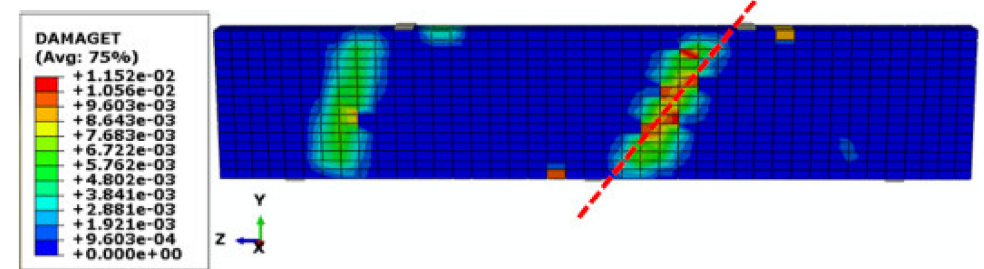
Figure 5. Cont.



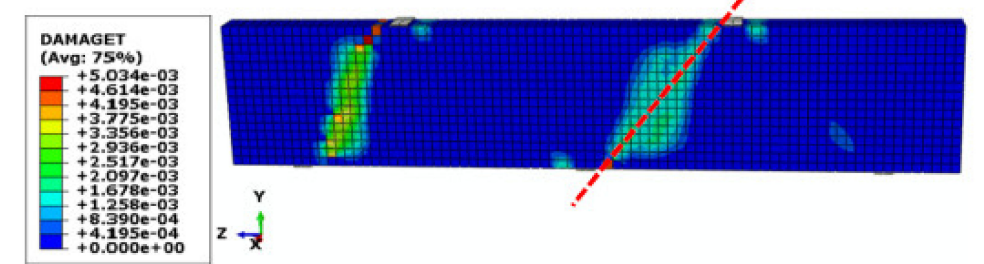
(f)



(g)

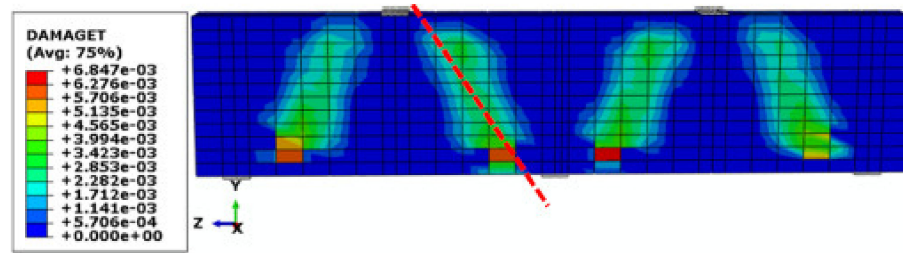


(h)



(i)

Figure 5. Cont.



(j)

Figure 6. Diagonal crack propagation in the deep beams: G1-300-N (a); G1-300-W (b); G1.7-300-N (c); G1.7-300-W (d); G1-600-N (e); G1-600-W (f); G1.7-600-W (g); G1-800-N (h); G1-800-W (i); S-600-N (j).

4. Results and Discussions

Table 3 presents the applied loads of the first flexural and diagonal cracks and failure load given by Zinkaah et al. [50] for the strengthened concrete deep beams. As per the results, the failure loads were obtained 5.6–8.7% time more often for the numerical models than for the experimental specimens.

Table 3. First flexural and diagonal cracks' loads based on the experimental outputs [50].

Specimen		G1-300-N	G1-300-W	G1.7-300-N	G1.7-300-W	G1-600-N	G1-600-W	G1.7-600-W	G1-800-N	G1-800-W	S1-600-N
First flexural cracking load (kN)	Mid-span	300	275	145	140	570	510	270	800	690	550
	Over middle support	270	250	145	140	540	500	270	780	680	540
Main diagonal cracking load (kN)		660	580	447	430	1150	945	785	1700	1490	1300
Failure load (kN)		937.3	1005.8	547.8	639.7	1388	1439.4	1000.5	1957.1	2050.3	1500.2

Since the maximum principal stress and von Mises stress, both of which are included in the ABAQUS program, are appropriate for assessing the non-linear performance of brittle and ductile materials, respectively, the concrete components and reinforcements' stress distribution were assessed using the maximum principal stress and von Mises stress, respectively, to achieve the reliable non-linear behaviour of the reinforced concrete deep beams. In addition, the evolution of damage in the failure zone of the numerical models was analyzed by means of the tensile damage variable (DAMAGET) plots, as displayed in Figure 6.

4.1. Flexural Performance of the Concrete Deep Beams with Different Heights

Figures 7–9 show the stress distributions in the GFRP-strengthened concrete deep beams with no web reinforcement and with heights of 300, 600, and 800 mm under applied loads of first flexural and diagonal cracks and failure load. It is noteworthy that the stress distribution in this study was the maximum tensile stress, but not the maximum absolute value of the stress.

Under the first flexural cracking load, the maximum stress in the concrete components with 300, 600, and 800 mm heights was equal to 1.68, 4.25, and 4.50 MPa, respectively, as indicated in Figures 7a, 8a and 9a. The corresponding values for the GFRP reinforcements were 2, 2.97, and 3.6 MPa, respectively. Therefore, by increasing the height of concrete deep beams from 300 mm to 600 mm and 800 mm, the maximum stress increased up to 2.5 and 2.7 times in the concrete component, respectively. Corresponding values were obtained of about 1.5 and 1.8 times for the GFRP reinforcement. In addition, under the first flexural cracking load, the highest stress intensity dissipated more along the length of the concrete

component with a height of 800 mm than that with heights of 300 and 600 mm. Therefore, the capacity of GFRP-strengthened concrete deep beams to carry the first flexural cracking load increased by increasing the height of the concrete deep beams. That is why the highest flexural cracking load was obtained for the GFRP-strengthened concrete deep beams with a height of 800 mm, as observed by Zinkaah et al. [50] (Table 3).

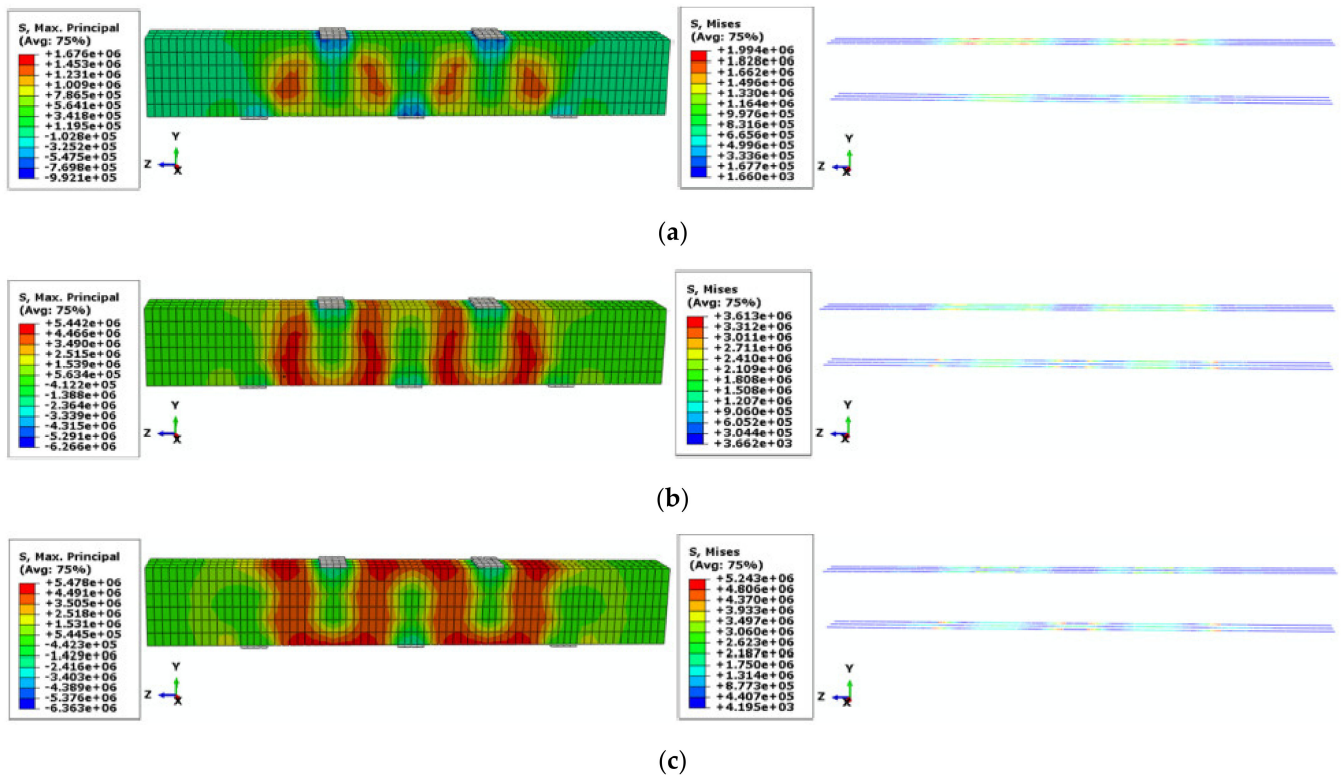


Figure 7. Stress distribution in the G1-300-N model under applied loads of first flexural (a) and diagonal (b) cracks; and failure load (c); the legends use the MPa unit.

As per Figures 7b, 8b and 9b, under the main diagonal cracking load, the concrete components' maximum tensile stress, including different heights, appeared to be between the interior support plate and the loading plates, in the range of 5.06–5.44 MPa. The tensile strength of concrete could be considered as about 10% of compressive strength [62,63], which was equal to 5.4 MPa, near to the same range obtained in this study, as mentioned earlier. Therefore, it can be inferred that the diagonal crack was propagated between the interior support plate and one of the loading plates, where the maximum tensile stress raised in the concrete components, similar to that observed in the plots of the tensile damage variable (DAMAGET) (Figure 6a,e,h).

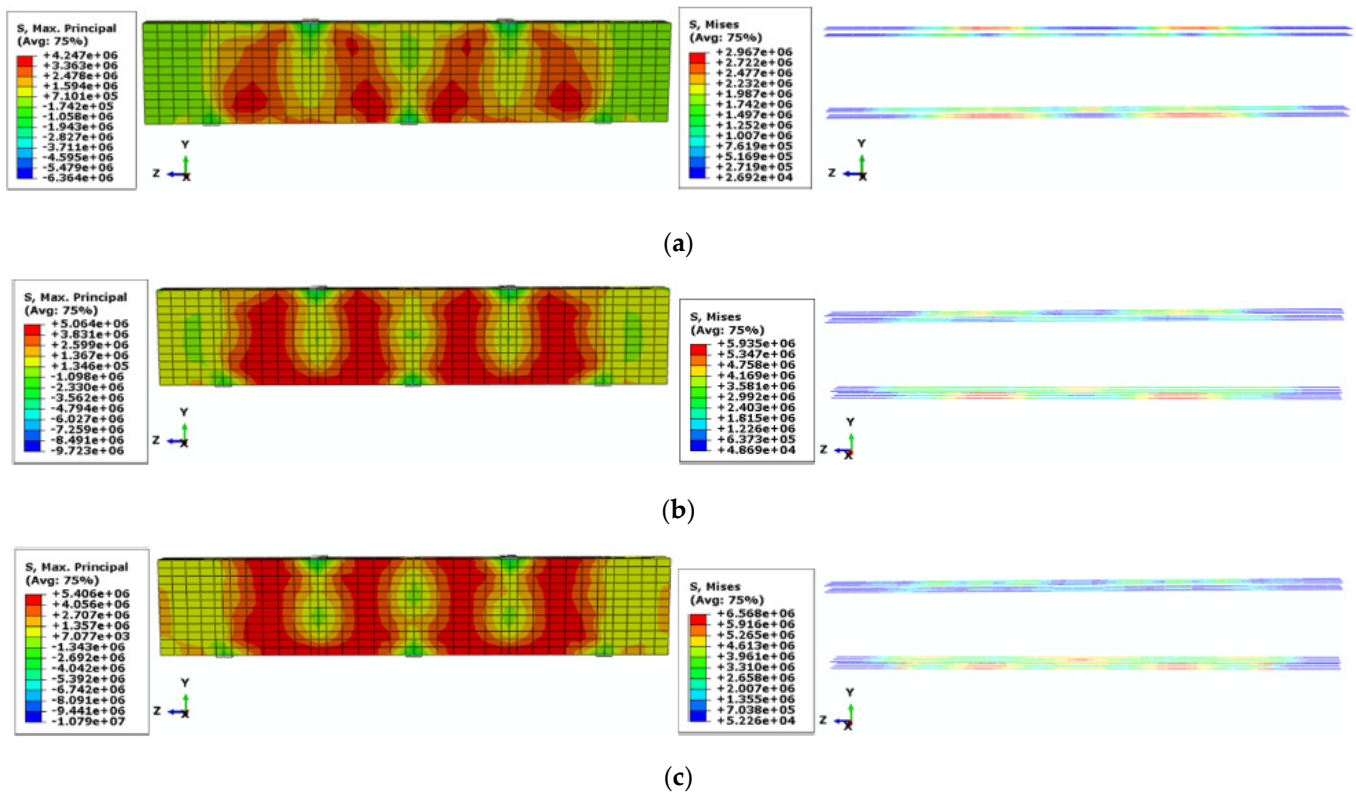


Figure 8. Stress distribution in the G1-600-N model under applied loads of first flexural (a) and diagonal (b) cracks; and failure load (c); the legends use the MPa unit.

As displayed in Figures 7c, 8c and 9c, up to the failure load, the highest stress intensity in concrete components dissipated more along the beam length and this dissipation appeared to be more for the concrete component with a height of 800 mm than that with heights of 300 and 600 mm. Furthermore, the maximum tensile stress propagated more in the bottom GFRP reinforcements than in the top GFRP reinforcements by increasing the load. This propagation occurred more for the GFRP rebars embedded in the concrete components with higher heights (600 and 800 mm). Therefore, GFRP reinforcements participated more in carrying the applied load by increasing the height of concrete deep beams.

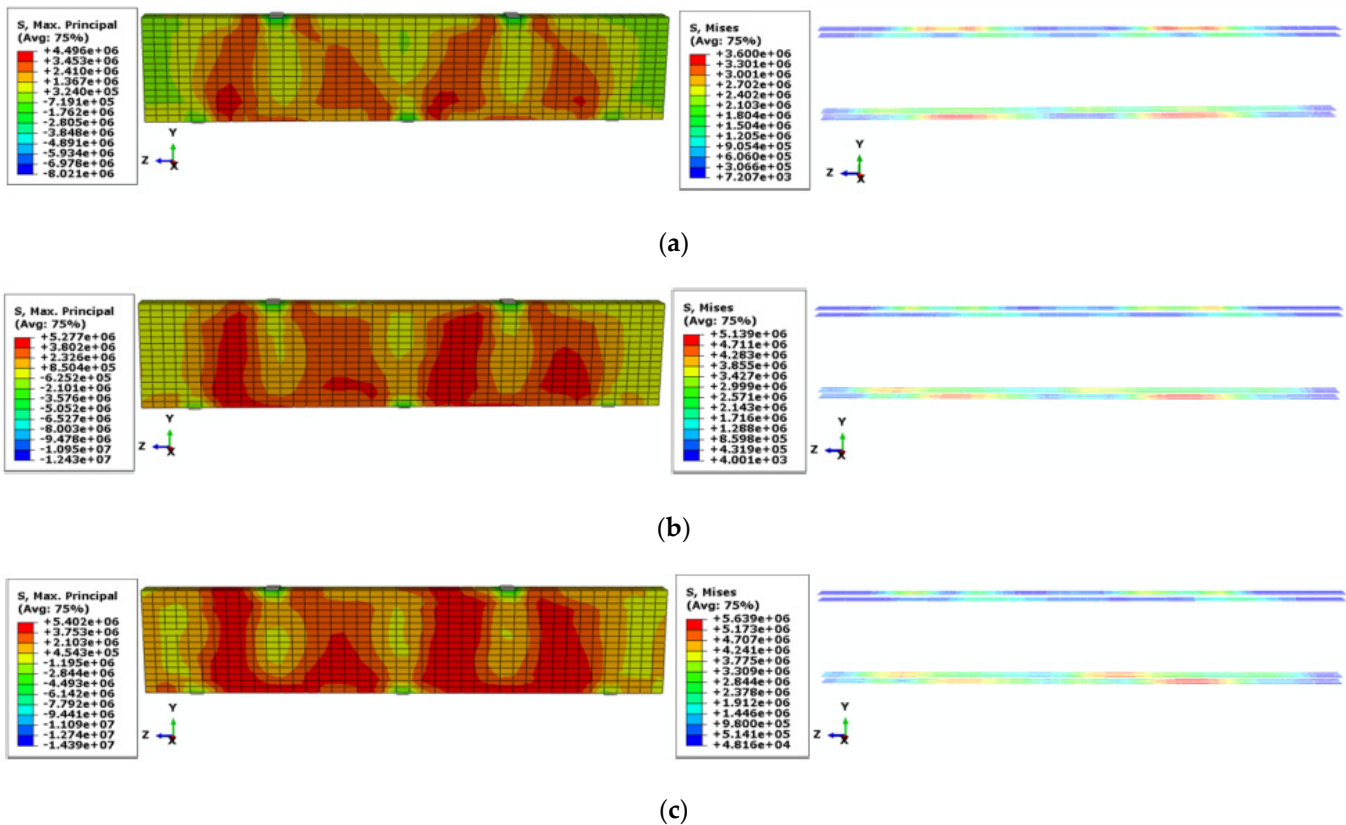


Figure 9. Stress distribution in the G1-800-N model under applied loads of first flexural (a) and diagonal (b) cracks; and failure load (c); the legends use the MPa unit.

4.2. Non-Linear Performance of Deep Beams Strengthened with Web GFRP Rebars

The stress distributions in the concrete deep beams with the web GFRP rebars under applied loads of first flexural and diagonal cracks and failure load are shown in Figures 10–12. The stress distribution was the maximum tensile stress, but not the maximum absolute value of the stress.

Under the first flexural cracking load, the maximum stress in the concrete components with the heights of 300, 600, and 800 mm was equal to 0.68, 3.12, and 3.48 MPa, respectively, as indicated in Figures 10a, 11a and 12a. The corresponding values for the GFRP reinforcements were 1.22, 3.37, and 3.64 MPa, respectively. Therefore, the maximum stress in the concrete and reinforcement components was improved by the height increment of the concrete deep beams with web GFRP reinforcement, similarly to what was observed for the concrete deep beams with the absence of web reinforcement (Figures 7a, 8a and 9a). However, the stress intensity in the concrete components was dissipated more along the beam length in the concrete deep beams with web reinforcement than in those with no web reinforcement. For instance, the web reinforcement collaborated with the concrete component to effectively dissipate the stress intensity along the whole length of the concrete deep beam with a height of 800 mm, as shown in Figure 12c.

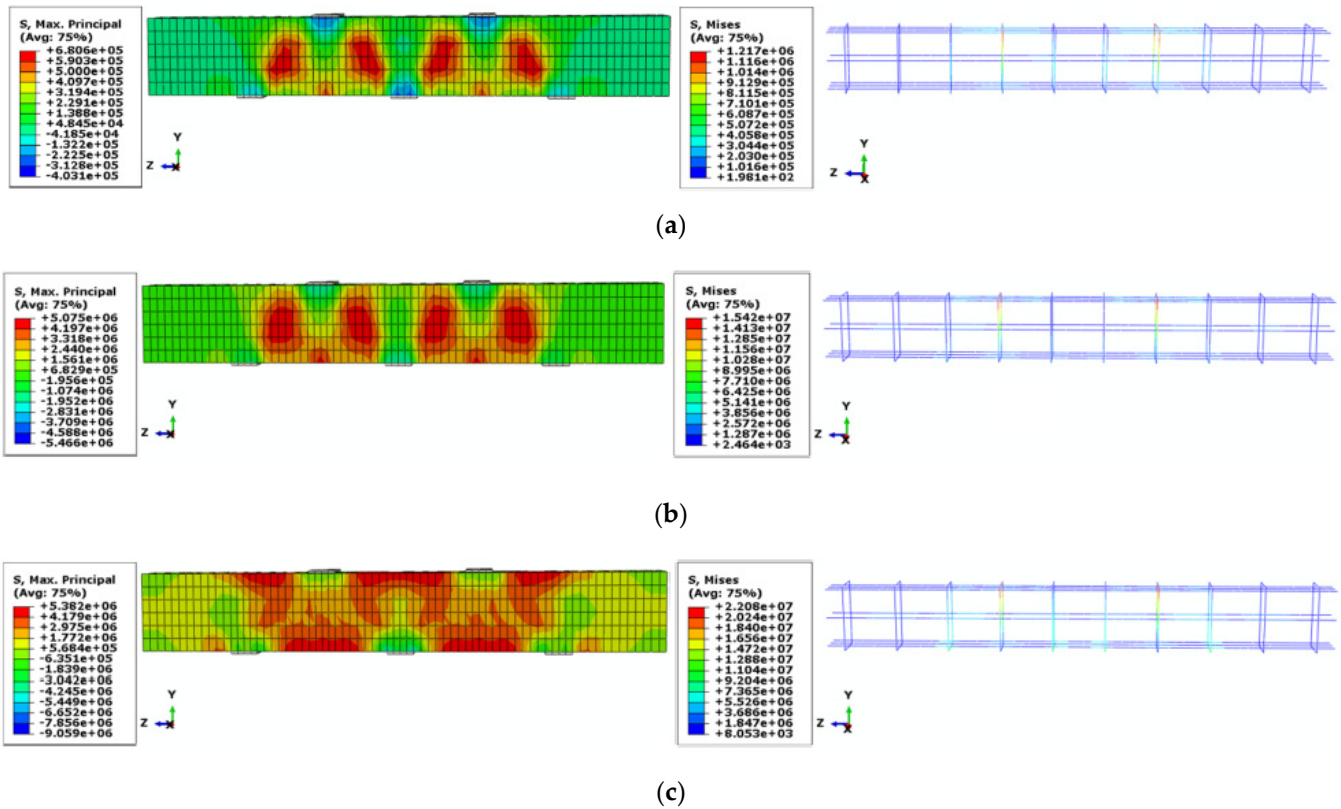


Figure 10. Stress distribution in the G1-300-W model under applied loads of first flexural (a) and diagonal (b) cracks; and failure load (c); the legends use the MPa unit.

The stress intensity was dissipated more in the web reinforcement embedded near to the bottom reinforcement than that embedded near to the top reinforcement, as shown in Figures 11 and 12. Therefore, the web reinforcement embedded near the bottom reinforcement participated more in carrying the applied load.

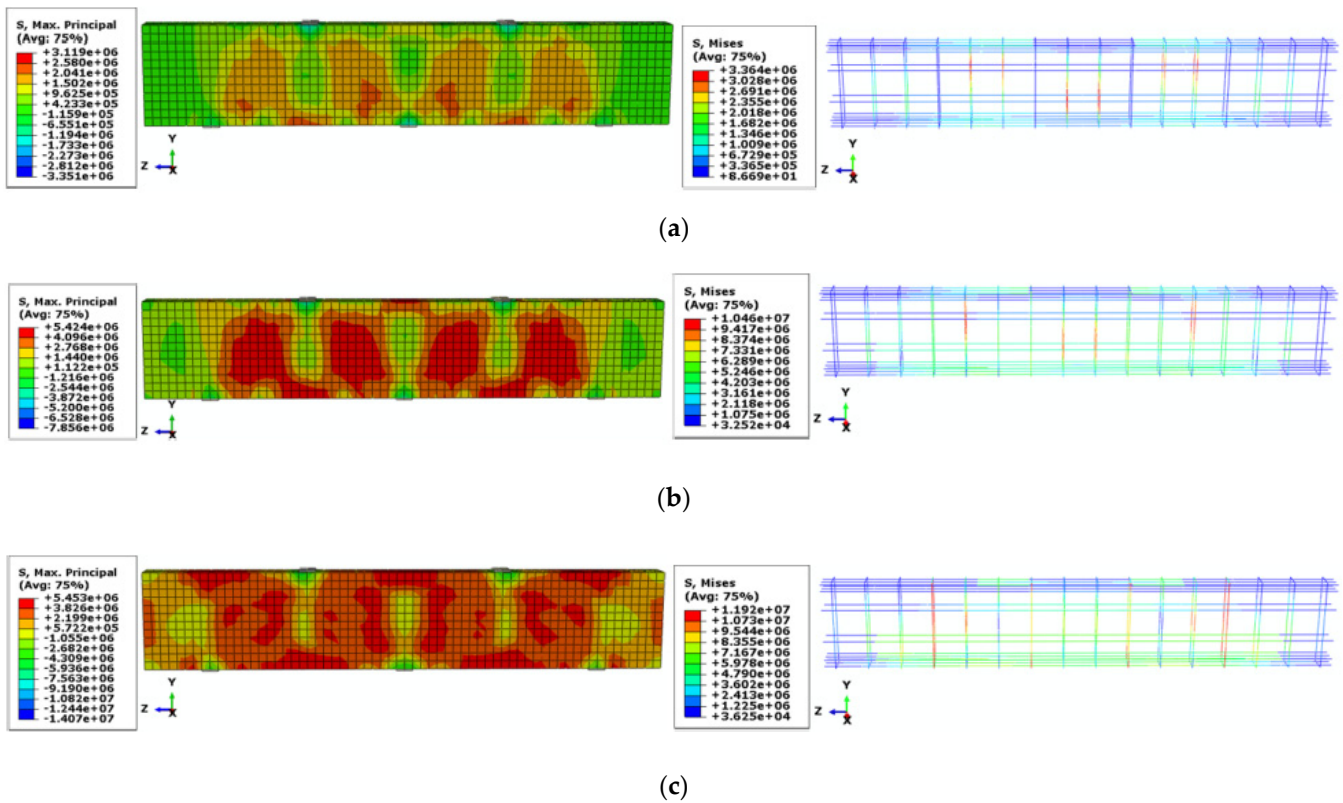


Figure 11. Stress distribution in the G1-600-W model under applied loads of first flexural (a) and diagonal (b) cracks; and failure load (c); the legends use the MPa unit.

Another matter is that the maximum tensile stress in the reinforcement of concrete deep beams with the web GFRP rebar under the failure load was in the 11.9–23.7 MPa range, as shown in Figures 10c, 11c and 12c. The corresponding range for the reinforcement of concrete deep beams without the web rebar was 5.2–6.5 MPa, as depicted in Figures 7c, 8c and 9c. Therefore, the presence of a web GFRP rebar increased the maximum tensile stress in the reinforcement and subsequently enhanced the participation of the reinforcement and concrete component in carrying a higher amount of loading. That is why the failure loads of concrete deep beams with the web GFRP rebar were moderately obtained, and more than those without the web GFRP rebar, as observed by Zinkaah et al. [50] (Table 3).

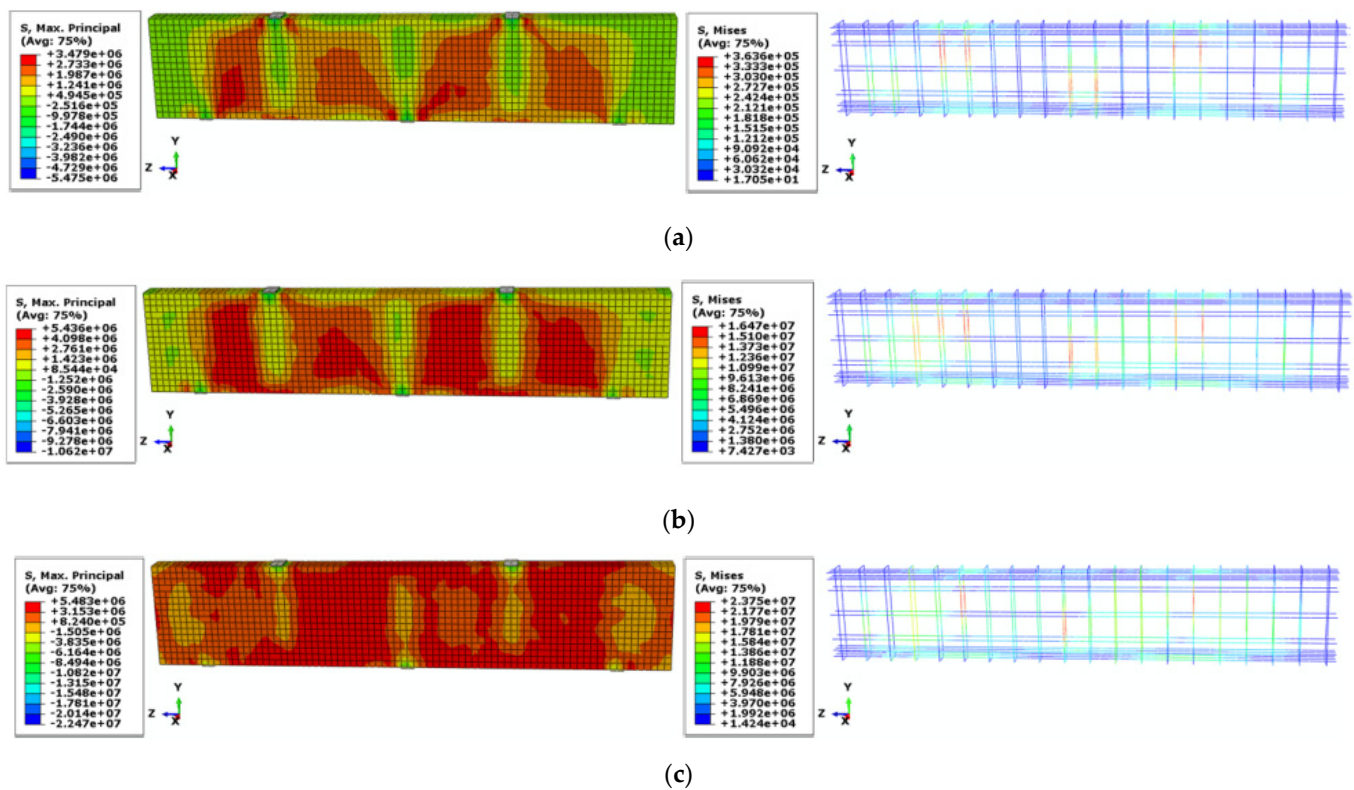


Figure 12. Stress distribution in the G1-800-W model under applied loads of first flexural (a) and diagonal (b) cracks; and failure load (c); the legends use the MPa unit.

4.3. Effect of a/h Ratio on the Stress Distribution in the Deep Beams

Figures 13–15 show the stress distributions of the GFRP-strengthened concrete deep beams with a higher a/h ratio (1.7). By increasing the a/h ratio from 1 to 1.7, the maximum stress in the concrete components of G1.7-300-N, G1.7-300-W, and G1.7-600-W models under the first flexural cracking load was equal to 1.08, 1.14, and 1.70 MPa, respectively, as indicated in Figures 13a, 14a and 15a. The corresponding values for the GFRP reinforcement were 3.39, 2.86, and 6.28 MPa, respectively. Therefore, the maximum stress in the GFRP-strengthened concrete deep beams with an a/h ratio of 1.7 under the first flexural cracking load increased with the presence of the web reinforcement, similarly to that observed for those with the a/h ratio of 1. However, the load-bearing capacity of GFRP-strengthened concrete deep beams decreased by increasing the a/h ratio from 1 to 1.7, as reported by Zinkaah et al. [50] (Table 3). This can be owing to the fact that the concrete is a brittle material with low tensile strength [64–83]. When the a/h ratio and length of concrete deep beams increased, the concrete component was unable to carry the higher amount of the flexural load, leading to a decrease in the load-carrying resistance of the GFRP-strengthened concrete deep beams.

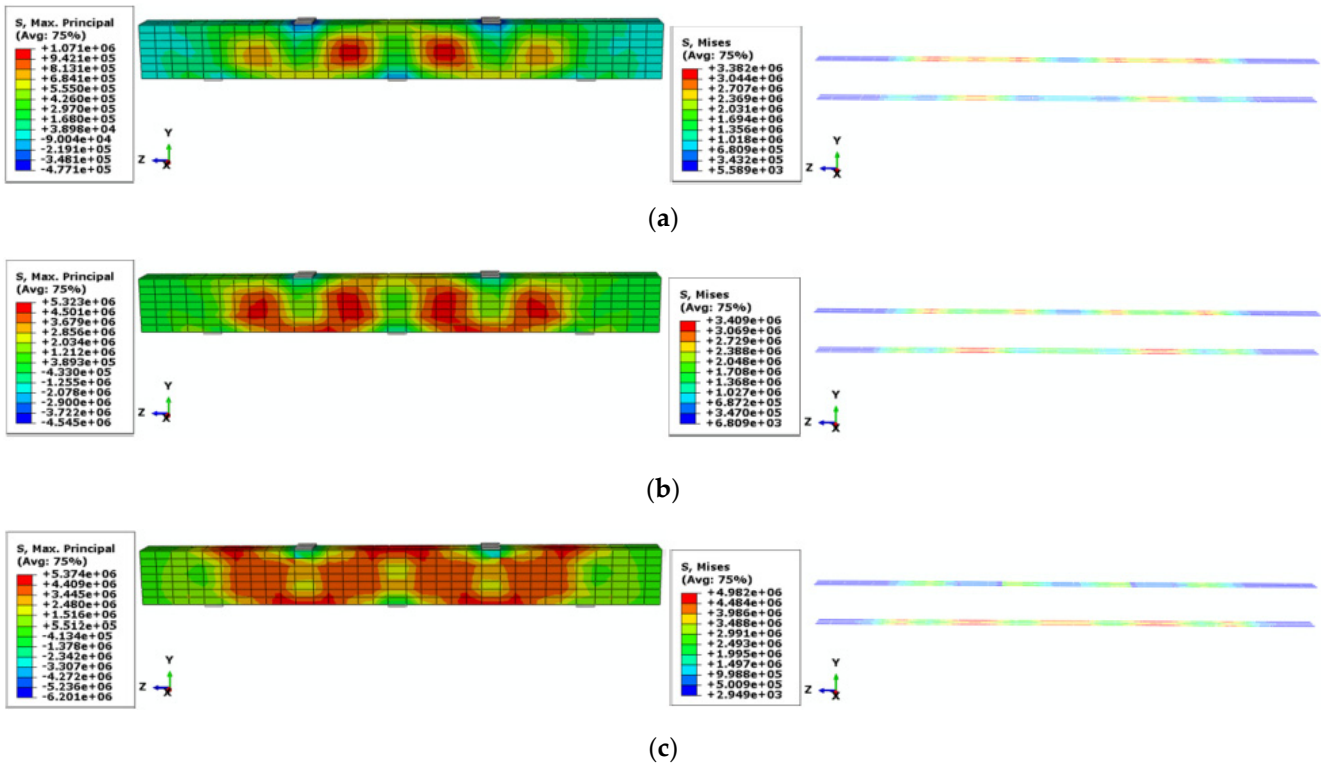


Figure 13. Stress distribution in the G1.7-300-N model under applied loads of first flexural (a) and diagonal (b) cracks; and failure load (c); the legends use the MPa unit.

As shown in Figures 13b, 14b and 15b, under main diagonal cracking load, the maximum tensile stress in the concrete components with different heights was in the 5.06–5.44 MPa range, where the diagonal crack appeared between the interior support plate and one of the loading plates, similar to that observed in the tensile damage variable plots (DAMAGET) (Figure 6c,d,g).

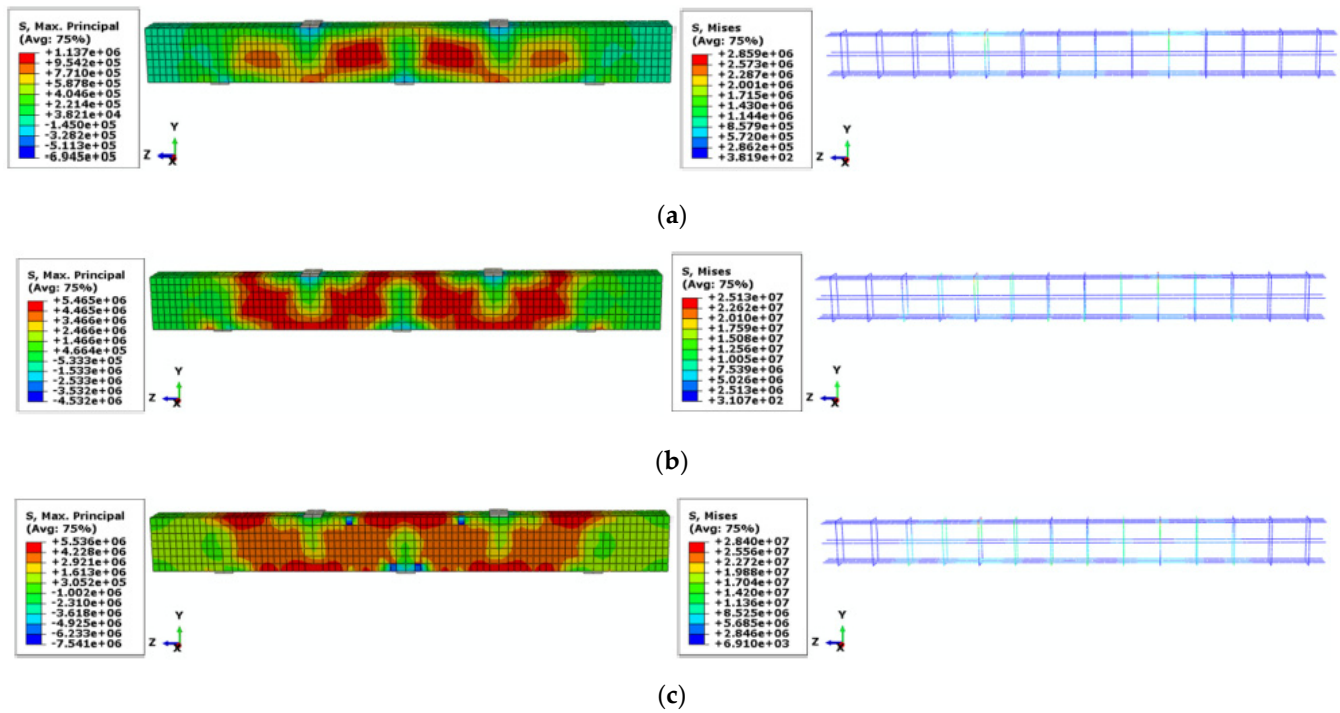


Figure 14. Stress distribution in the G1.7-300-W model under applied loads of first flexural (a) and diagonal (b) cracks; and failure load (c); the legends use the MPa unit.

Under failure load, the maximum tensile stresses in the reinforcements of G1.7-300-N, G1.7-300-W, and G1.7-600-W models increased by 4.98, 28.4, and 48 MPa as shown in Figures 13c, 14c and 15c, respectively. These values showed that the participation of the combined reinforcement and concrete components in carrying the applied load was remarkably increased by the web reinforcement presence and by increasing the height of concrete deep beams, similar to that observed by Thomas and Ramadass [47] for concrete deep beams strengthened with FRP rebars.

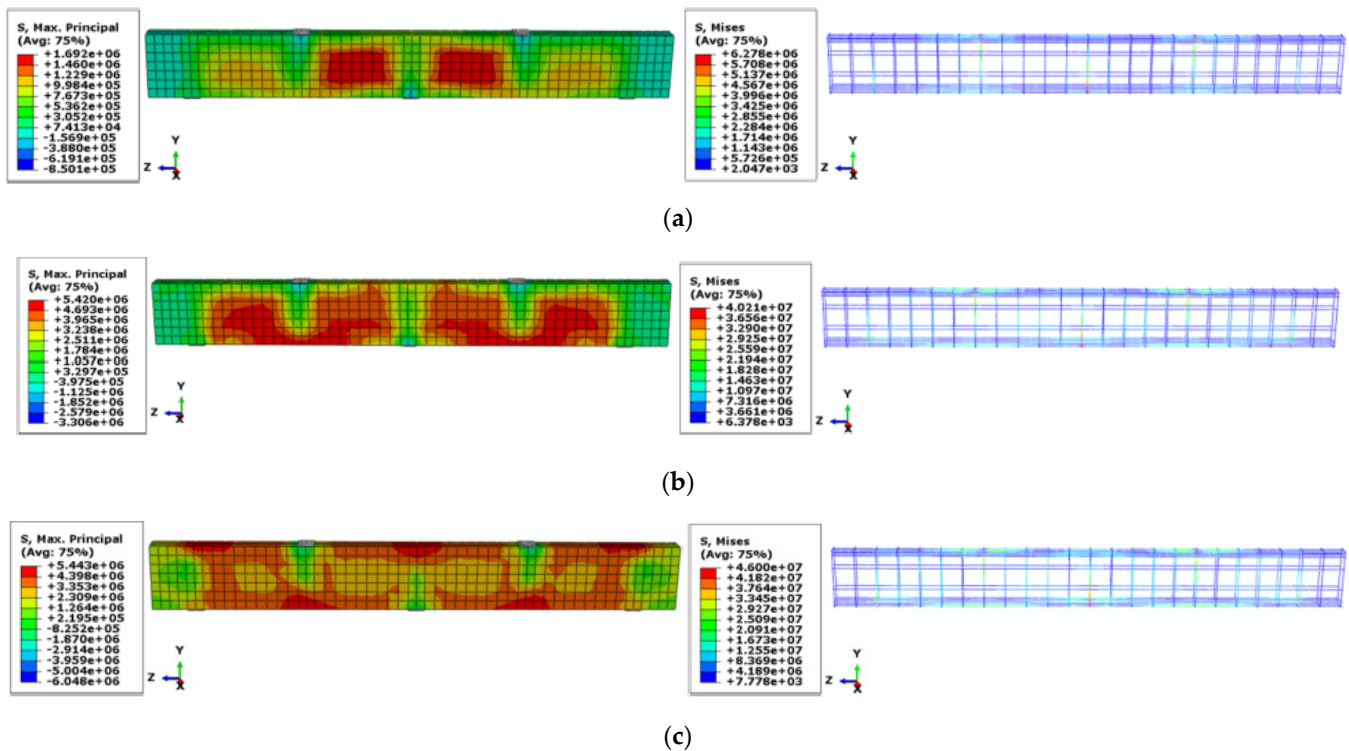


Figure 15. Stress distribution in the G1.7-600-W model under applied loads of first flexural (a) and diagonal (b) cracks; and failure load (c); the legends use the MPa unit.

4.4. Effect of Steel, GFRP, and CFRP Longitudinal Reinforcements on the Non-Linear Performance of Deep Beams

The total load against mid-span deflection curves of the concrete deep beams with 600-mm height and reinforced with longitudinal steel, GFRP, and CFRP rebars were compared to each other, as depicted in Figure 16. As per the results, the concrete deep beams strengthened with GFRP, CFRP, and steel top and bottom reinforcements failed up to 1462, 1532, and 1621 MPa, respectively. Therefore, the ultimate load-carrying resistance of the concrete beams with a height of 600 mm and without the web reinforcement increased by up to 4.8% and 10.9% by replacing the GFRP reinforcement with the CFRP and steel reinforcements, respectively.

The stress distributions in the concrete deep beams strengthened with the longitudinal GFRP, CFRP, and steel rebars under failure load are presented in Figures 8c, 17a and 16b, respectively. The maximum tensile stress in the concrete components of deep beams reinforced with different types of reinforcements was near 5.4 MPa. However, the stress intensity in the concrete components of deep beams strengthened with the steel reinforcement (S1-600-N) was moderately dissipated along the beam length more than that in the concrete deep beams with the CFRP reinforcement (C1-600-N). This intensity was slightly dissipated more in the concrete component of the deep beam reinforced with the CFRP reinforcement (C1-600-N) than that strengthened with the GFRP reinforcement (G1-600-N). On the other hand, the maximum tensile stresses in GFRP, CFRP, and steel reinforcements of the deep beams were equal to 6.57, 16.2, and 23 MPa, as shown in Figures 8c and 17a,b, respectively. Therefore, the highest stress intensity appeared to be more in the CFRP and steel rebars than the GFRP rebar, which can be owing to the fact that the modulus of elasticity of CFRP and steel rebars was remarkably more than that of the GFRP rebar (Table 2), leading to the higher dowel action of the steel and CFRP rebars than that of the GFRP rebar, similarly to that reported by other researchers [1,50,84].

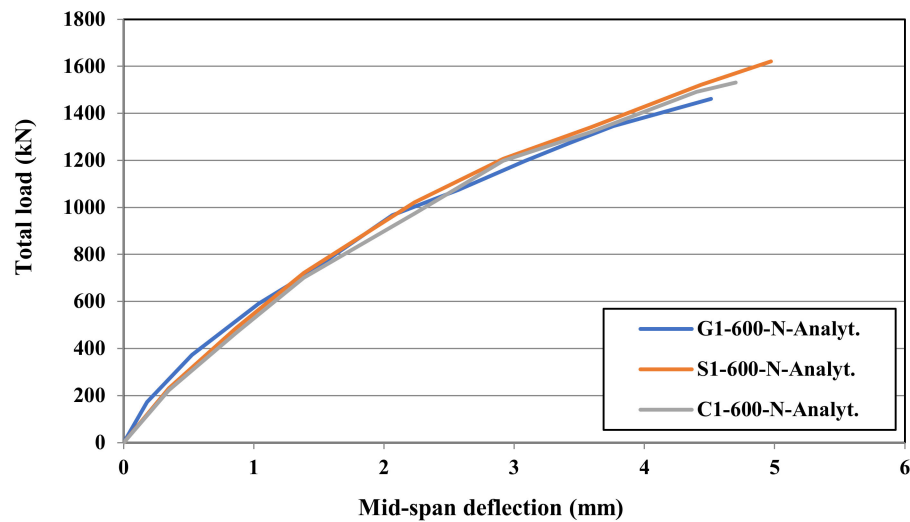


Figure 16. Load vs. mid-span deflection plot for specimens strengthened with longitudinal steel, GFRP, and CFRP rebars.

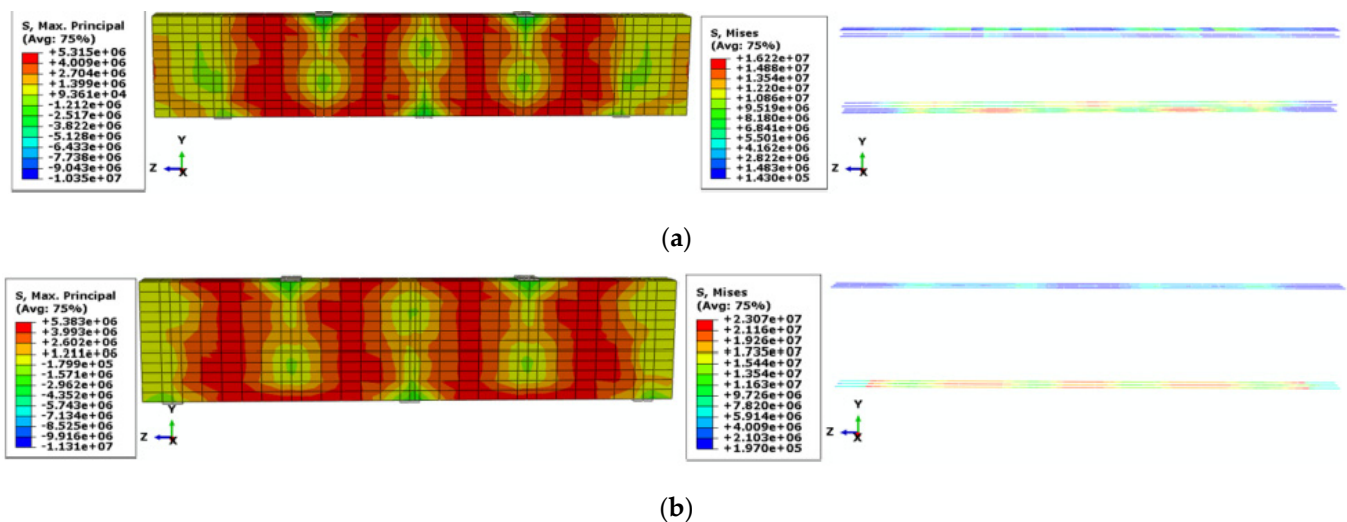


Figure 17. Stress distribution in the C1-600-N (a); and S1-600-N (b) models under failure load; the legends use the MPa unit.

4.5. Non-Linear Performance of the Deep Beams without Top Longitudinal Reinforcement

Figure 18 shows a comparison between the curves of total load against mid-span deflection for the concrete deep beams with and without top longitudinal reinforcement. With the absence of the web reinforcement, the failure loads of the concrete deep beams with and without the top reinforcement were equal to 1462 and 1331 MPa, respectively. The corresponding values for the concrete deep beams with the presence of the web reinforcement were 1527 and 1449 MPa. Therefore, with the absence of the web reinforcement, the failure load was obtained 8.7% more for the concrete deep beam with the top reinforcement (G1-600-N) than that without the top reinforcement (G1-600-N-AT). The corresponding difference was 5.4% with the presence of web reinforcement. It can be stated that the web reinforcement slightly compensated for the absence of the top rebar to reinforce the concrete deep beams in carrying the ultimate load.

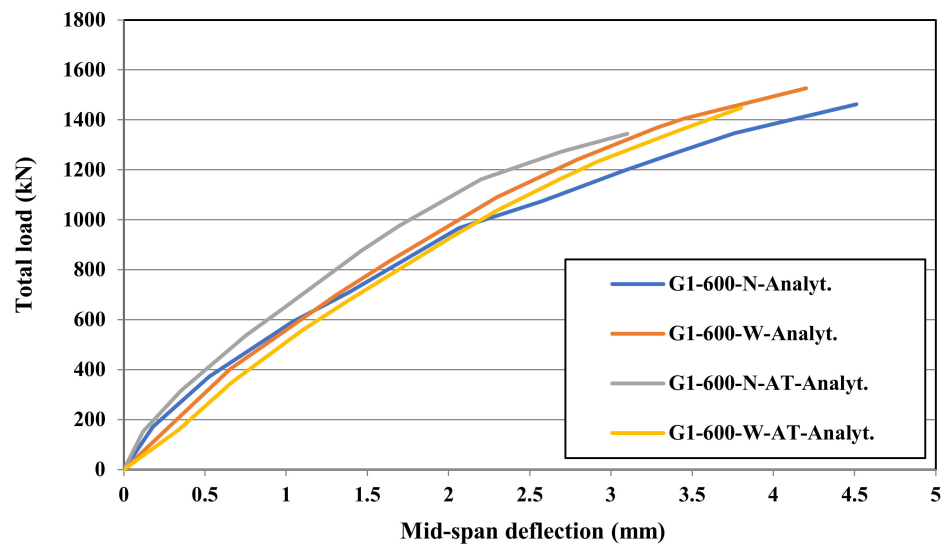


Figure 18. Load vs. mid-span deflection plot for the deep beams reinforced with and without top reinforcements.

The stress distributions in the concrete deep beams without the top longitudinal reinforcement under failure load are depicted in Figure 19. As per the results, the maximum tensile stress propagation along the beam length of the concrete component without the top reinforcement (Figure 19) was not as much as that of the concrete component with the top reinforcement (Figures 8c and 11c). In addition, with the absence of the top reinforcement, the maximum tensile stresses in the reinforcements of deep beams with and without the web rebar were 11.27 and 6.26 MPa, respectively, which showed that the maximum tensile stress was dissipated more in the concrete component of the deep beam with the web rebar than that without the web rebar (Figure 19). That is why the failure load of the concrete deep beam with the web rebar was obtained by 7.7% more than that without the web rebar when there was no top reinforcement, as presented in Figure 18. It is noteworthy that the stress intensity was dissipated more in the web reinforcement embedded near to the top reinforcement than that embedded near to the bottom reinforcement, as shown in Figure 19b.

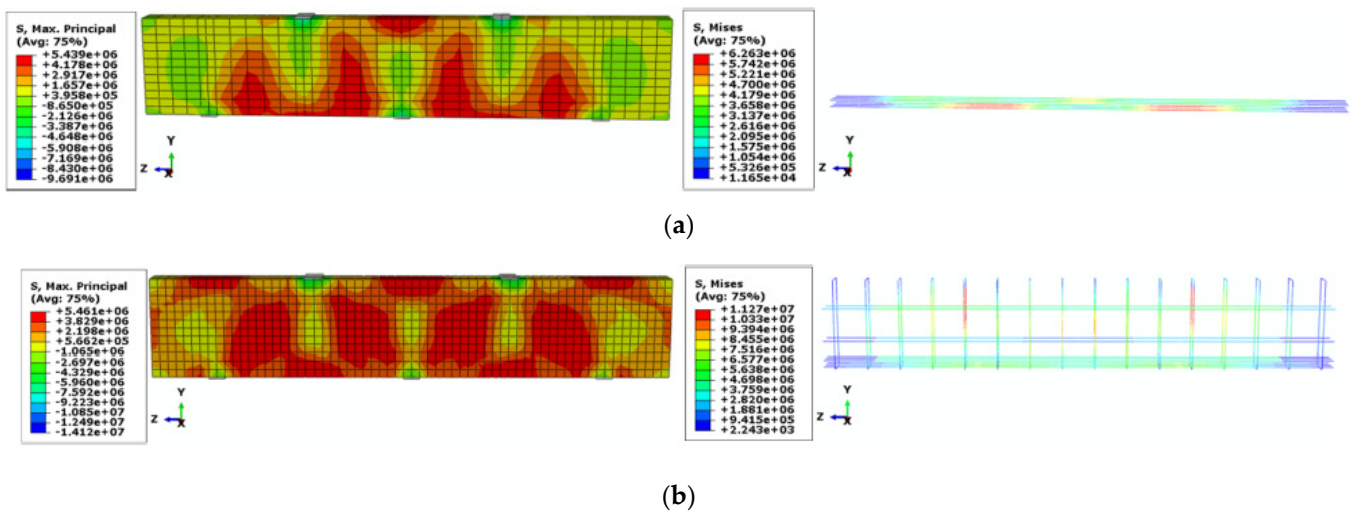


Figure 19. Stress spreading in the G1-600-N-AT (a); and G1-600-W-AT (b) models under failure load; the legends use the MPa unit.

4.6. A Comparison between the GFRP Strengthened High- and Normal-Strength Concrete Deep Beams

The curves of total load against mid-span deflection of the high- and normal-strength concrete deep beams with 600-mm height and reinforced with GFRP rebars are presented in Figure 20. The results showed that the failure loads of the high-strength concrete deep beams with and without the web reinforcement were obtained as 16.4% and 22.3%, respectively, more than those of the normal-strength concrete deep beams, and similarly to those reported by Khorasani and Esfahani [85] for conventional concrete beams strengthened with the GFRP rebar. It can be stated that the difference between the results of high- and normal-strength concrete deep beams with the web reinforcement (16.4%) was lower than that without the web reinforcement (22.3%). Therefore, the web reinforcement could somewhat compensate for the lower strength of the normal concrete to strengthen the deep beams in carrying the ultimate load.

The high-strength concrete impact on the deep beams' stress distribution with a height of 600 mm under failure load is depicted in Figure 21. The maximum tensile stress in the normal-strength concrete component under failure load was nearly equal to 3 MPa (about 10% of the compressive strength of normal concrete), as depicted in Figure 21. The corresponding value was about 5.4 MPa for the high-strength concrete components (Figures 8c and 11c). In addition, the maximum tensile stresses in the reinforcement of the normal-strength concrete deep beams with and without the web reinforcement were 8.18 and 4.33 MPa, as shown in Figure 21a,b, respectively. The corresponding values for the high-strength concrete deep beams were 11.92 and 6.57 MPa, as depicted in Figures 8c and 11c, respectively. It can be stated that the maximum tensile stresses in the reinforcement of high-strength concrete deep beams with and without the web reinforcement were 45.7% and 51.5% more than those of the high-strength concrete deep beams. Therefore, the GFRP reinforcement and the high-strength concrete participation was more than that of the GFRP reinforcement and the normal-strength concrete. This participation triggered a scattering of the maximum tensile stress along the length of the high-strength concrete component, greater than that of the normal-strength concrete component, leading to an increase in the load-carrying capacity of the high-strength concrete deep beams.

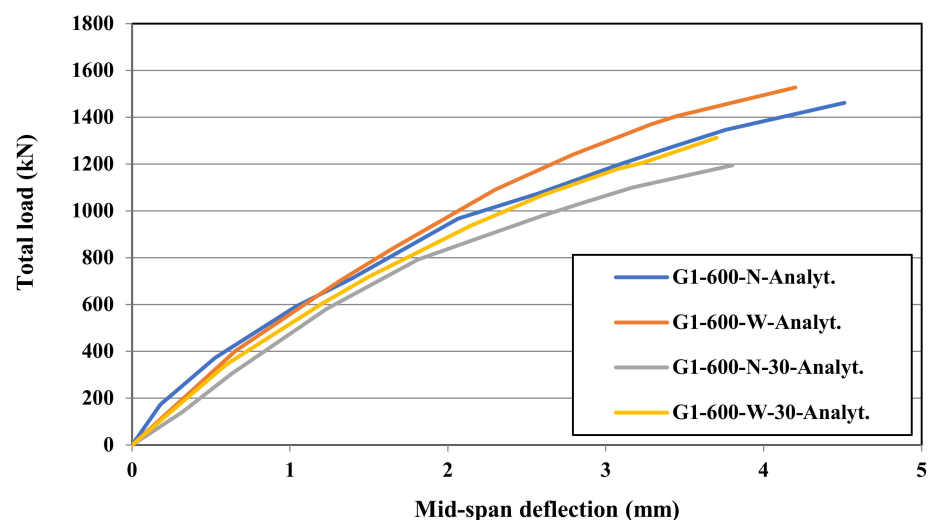


Figure 20. Load vs. mid-span deflection plot for the GFRP reinforced high- and normal-strength concrete deep beams.

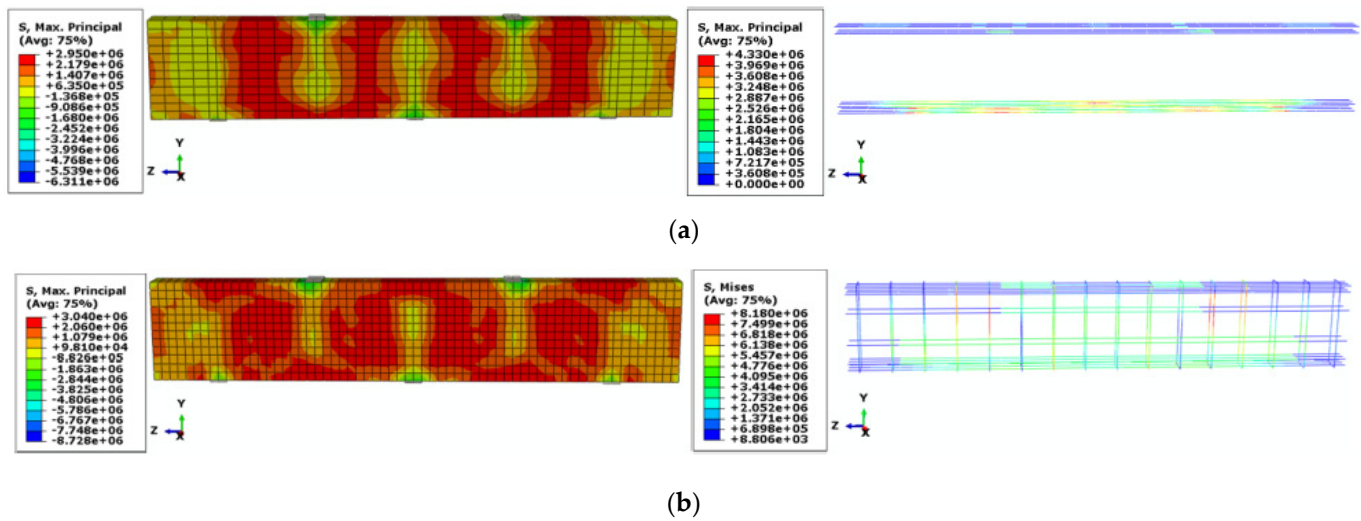


Figure 21. Stress spreading in the G1-600-N-30 (a); and G1-600-W-30 (b) models under failure load; the legends use the MPa unit.

5. Conclusions

In this study, the numerical analyses evaluated the impact of the concrete strength and top and web longitudinal reinforcements on the non-linear behaviour of GFRP- and CFRP-strengthened concrete deep beams. The following conclusions can be formed based on the numerical outputs:

- The maximum tensile stress was propagated more in the bottom GFRP reinforcements than the top GFRP reinforcements by increasing the load. In addition, the highest dissipation of stress intensity along the beam length was observed for the concrete component with a height of 800 mm. Therefore, the participation of GFRP reinforcements and concrete component increased by increasing the height of concrete deep beams to carry the applied load.
- The stress intensity in the concrete components was dissipated along the beam length more in the concrete deep beams with the web reinforcement than those with no web reinforcement. This intensity was dissipated more in the web reinforcement embedded near to the bottom reinforcement than that embedded near to the top reinforcement.
- The maximum tensile stress in the reinforcement of concrete deep beams with the web GFRP rebar under the failure load was obtained in the range of 11.9–23.7 MPa. The corresponding range for the reinforcement of concrete deep beams without the web rebar was 5.2–6.5 MPa. Therefore, the presence of web GFRP rebar increased the maximum tensile stress in the rebar component and subsequently enhanced the participation of the reinforcement and concrete component in carrying a higher amount of loading.
- By the presence of the web reinforcement and by increasing the height of the concrete deep beams, the participation of the combined reinforcement and concrete components in carrying the applied load increased for the concrete deep beams with a/h ratio of 1.7, but not as much as those with a/h ratio of 1.
- By replacing the GFRP reinforcement with CFRP and steel reinforcements, the ultimate load-bearing resistance of concrete beams with the 600-mm height and without the web reinforcement increased up to 4.8% and 10.9%, respectively.
- The maximum tensile stresses in the GFRP, CFRP, and steel reinforcements were equal to 6.57, 16.2, and 23 MPa, respectively. Therefore, the highest tensile stress was obtained for the steel reinforcement and the tensile stress in the CFRP reinforcement was obtained more than that in the GFRP reinforcement under the failure load. In addition, the stress intensity in the concrete components of deep beams reinforced with the steel reinforcement (S1-600-N) was moderately dissipated along the beam length

more than that in the concrete deep beams with the CFRP and GFRP reinforcements (C1-600-N and G1-600-N).

- With the absence of the web reinforcement, the failure load of the concrete deep beam with the top reinforcement (G1-600-N) was 8.7% more than that without the top reinforcement (G1-600-N-AT). The corresponding difference was 5.4% with the presence of the web reinforcement. Therefore, the web reinforcement slightly compensated for the absence of the top rebar to reinforce the concrete deep beams in carrying the ultimate load.
- The maximum tensile stress distribution along the beam length of the concrete component without the top reinforcement was not as much as that of the concrete component with the top reinforcement. In addition, with the absence of the top reinforcement, the maximum tensile stress was dissipated more in the concrete deep beam with the web rebar than that without the web rebar.
- With the absence of the top reinforcement, the stress intensity in the web reinforcement embedded near to the top reinforcement was more than that near to the bottom reinforcement, contrarily to the concrete deep beams with the presence of the top reinforcement.
- The difference between the results of high- and normal-strength concrete deep beams with the web reinforcement (16.4%) was lower than that without the web reinforcement (22.3%). Therefore, the web reinforcement moderately compensated for the low strength of the normal concrete in strengthening the deep beams in carrying the ultimate load.
- The maximum tensile stresses in the reinforcement of the high-strength concrete deep beams were 45.7% and 51.5% more than those of the high-strength concrete deep beams with the presence and absence of the web reinforcement, respectively. Therefore, the participation of the GFRP reinforcement with the high-strength concrete was more than that with the normal-strength concrete in carrying a higher amount of loading.

In general, as an applicable structural member, in some cases the exposure of reinforced concrete deep beams to a corrosive environment is inevitable, which can lead to the corrosion of steel reinforcement rebars. The widespread use of FRP reinforcement rebars would contribute to addressing this problem; thus, this study used the numerical modeling outputs to shed some light on the effects of the concrete strength, top and web longitudinal reinforcements, and types of FRP flexural rebars on the non-linear performance of numerical models to provide more sustainable concrete deep beams for the construction sector.

Author Contributions: M.K.: conceptualization, methodology, software, validation, formal analysis, investigation, data curation, writing—original draft preparation; M.D.: formal analysis, investigation, writing—review and editing; Y.Z., A.S.A., N.Y., L.M., A.R., M.S., A.M., M.A.K., J.L.: writing—review and editing. All authors have read and agreed to the published version of the manuscript.

Funding: This research received no external funding.

Institutional Review Board Statement: Not applicable.

Informed Consent Statement: Not applicable.

Data Availability Statement: Not applicable.

Conflicts of Interest: The authors declare no conflict of interest.

References

1. Abed, F.; El-Chabib, H.; AlHamaydeh, M. Shear Characteristics of GFRP-Reinforced Concrete Deep Beams without Web Reinforcement. *J. Reinf. Plast. Compos.* **2012**, *31*, 1063–1073. [[CrossRef](#)]
2. Kachouh, N.; El-Maaddawy, T.; El-Hassan, H.; El-Ariss, B. Shear Response of Recycled Aggregates Concrete Deep Beams Containing Steel Fibers and Web Openings. *Sustainability* **2022**, *14*, 945. [[CrossRef](#)]
3. Fang, Q.; Wang, G.; Yu, F.; Du, J. Analytical Algorithm for Longitudinal Deformation Profile of a Deep Tunnel. *J. Rock Mech. Geotech. Eng.* **2021**, *13*, 845–854. [[CrossRef](#)]

4. Jarrah, M.; Najafabadi, E.P.; Khaneghahi, M.H.; Oskouei, A.V. The Effect of Elevated Temperatures on the Tensile Performance of GFRP and CFRP Sheets. *Constr. Build. Mater.* **2018**, *190*, 38–52. [[CrossRef](#)]
5. Kazemi, M.; Li, J.; Harehdasht, S.L.; Yousefieh, N.; Jahandari, S.; Saberian, M. Non-Linear Behaviour of Concrete Beams Reinforced with GFRP and CFRP Bars Grouted in Sleeves. In Proceedings of the Structures; Elsevier: Amsterdam, The Netherlands, 2020; Volume 23, pp. 87–102.
6. Rahif, R.; Amaripadath, D.; Attia, S. Review on Time-Integrated Overheating Evaluation Methods for Residential Buildings in Temperate Climates of Europe. *Energy Build.* **2021**, *252*, 111463. [[CrossRef](#)]
7. Kazemi, M.; Courard, L.; Hubert, J. Coarse Recycled Materials for the Drainage and Substrate Layers of Green Roof System in Dry Condition: Parametric Study and Thermal Heat Transfer. *J. Build. Eng.* **2022**, *45*, 103487. [[CrossRef](#)]
8. Kazemi, M.; Courard, L.; Hubert, J. Heat Transfer Measurement within Green Roof with Incinerated Municipal Solid Waste Aggregates. *Sustainability* **2021**, *13*, 7115. [[CrossRef](#)]
9. Kazemi, M.; Courard, L. Modelling Hygrothermal Conditions of Unsaturated Substrate and Drainage Layers for the Thermal Resistance Assessment of Green Roof: Effect of Coarse Recycled Materials. *Energy Build.* **2021**, *250*, 111315. [[CrossRef](#)]
10. Pilechiha, P.; Norouzasias, A.; Ghorbani Naeini, H.; Jolma, K. Evaluation of Occupant's Adaptive Thermal Comfort Behaviour in Naturally Ventilated Courtyard Houses. *Smart Sustain. Built Environ.* **2021**. *ahead-of-print*. [[CrossRef](#)]
11. Miraki, H.; Shariatmadari, N.; Ghadir, P.; Jahandari, S.; Tao, Z.; Siddique, R. Clayey Soil Stabilization Using Alkali-Activated Volcanic Ash and Slag. *J. Rock Mech. Geotech. Eng.* **2021**, *14*, 1–16. [[CrossRef](#)]
12. Hataf, N.; Ghadir, P.; Ranjbar, N. Investigation of Soil Stabilization Using Chitosan Biopolymer. *J. Clean. Prod.* **2018**, *170*, 1493–1500. [[CrossRef](#)]
13. Mou, B.; Bai, Y. Experimental Investigation on Shear Behavior of Steel Beam-to-CFST Column Connections with Irregular Panel Zone. *Eng. Struct.* **2018**, *168*, 487–504. [[CrossRef](#)]
14. Sinaei, H.; Jumaat, M.Z.; Shariati, M. Numerical Investigation on Exterior Reinforced Concrete Beam-Column Joint Strengthened by Composite Fiber Reinforced Polymer (CFRP). *Int. J. Phys. Sci.* **2011**, *6*, 6572–6579.
15. Zhang, C.; Abedini, M. Development of P-I Model for FRP Composite Retrofitted RC Columns Subjected to High Strain Rate Loads Using LBE Function. *Eng. Struct.* **2022**, *252*, 113580. [[CrossRef](#)]
16. Huang, H.; Xue, C.; Zhang, W.; Guo, M. Torsion Design of CFRP-CFST Columns Using a Data-Driven Optimization Approach. *Eng. Struct.* **2022**, *251*, 113479. [[CrossRef](#)]
17. Wei, J.; Xie, Z.; Zhang, W.; Luo, X.; Yang, Y.; Chen, B. Experimental Study on Circular Steel Tube-Confined Reinforced UHPC Columns under Axial Loading. *Eng. Struct.* **2021**, *230*, 111599. [[CrossRef](#)]
18. Sajedi, F.; Shariati, M. Behavior Study of NC and HSC RCCs Confined by GRP Casing and CFRP Wrapping. *Steel Compos. Struct* **2019**, *30*, 417–432.
19. Xiao, X.; Bu, G.; Ou, Z.; Li, Z. Nonlinear In-Plane Instability of the Confined FGP Arches with Nanocomposites Reinforcement under Radially-Directed Uniform Pressure. *Eng. Struct.* **2022**, *252*, 113670. [[CrossRef](#)]
20. Sadeghian, F.; Haddad, A.; Jahandari, S.; Rasekh, H.; Ozbakkaloglu, T. Effects of Electrokinetic Phenomena on the Load-Bearing Capacity of Different Steel and Concrete Piles: A Small-Scale Experimental Study. *Can. Geotech. J.* **2021**, *58*, 741–746. [[CrossRef](#)]
21. Cheng, H.; Sun, L.; Wang, Y.; Chen, X. Effects of Actual Loading Waveforms on the Fatigue Behaviours of Asphalt Mixtures. *Int. J. Fatigue* **2021**, *151*, 106386. [[CrossRef](#)]
22. Dong, J.; Deng, R.; Quanying, Z.; Cai, J.; Ding, Y.; Li, M. Research on Recognition of Gas Saturation in Sandstone Reservoir Based on Capture Mode. *Appl. Radiat. Isot.* **2021**, *178*, 109939. [[CrossRef](#)] [[PubMed](#)]
23. Roudi, A.; Chelliapan, S.; Kamyab, H.; Md Din, M.F.; Krishnan, S. Removal of COD from Landfill Leachate by Predication and Evaluation of Multiple Linear Regression (MLR) Model and Fenton Process. *Egypt. J. Chem.* **2019**, *62*, 1207–1218. [[CrossRef](#)]
24. Zhang, S.; Pak, R.Y.S.; Zhang, J. Three-Dimensional Frequency-Domain Green's Functions of a Finite Fluid-Saturated Soil Layer Underlain by Rigid Bedrock to Interior Loadings. *Int. J. Geomech.* **2022**, *22*, 04021267. [[CrossRef](#)]
25. Lu, N.; Wang, H.; Wang, K.; Liu, Y. Maximum Probabilistic and Dynamic Traffic Load Effects on Short-to-Medium Span Bridges. *Comput. Modeling Eng. Sci.* **2021**, *127*, 345–360. [[CrossRef](#)]
26. Zhang, H.; Liu, Y.; Deng, Y. Temperature Gradient Modeling of a Steel Box-Girder Suspension Bridge Using Copulas Probabilistic Method and Field Monitoring. *Adv. Struct. Eng.* **2021**, *24*, 947–961. [[CrossRef](#)]
27. Xiang, G.X.; Gao, X.; Tang, W.J.; Jie, X.Z.; Huang, X. Numerical Study on Transition Structures of Oblique Detonations with Expansion Wave from Finite-Length Cowl. *Phys. Fluids* **2020**, *32*, 056108. [[CrossRef](#)]
28. Akbarzadeh Bengar, H.; Shahmansouri, A.A. A New Anchorage System for CFRP Strips in Externally Strengthened RC Continuous Beams. *J. Build. Eng.* **2020**, *30*, 101230. [[CrossRef](#)]
29. Kazemi, M.; Madandoust, R.; Chastre, C.; Reza Esfahani, M.; Courard, L. Numerical Study on the Flexural Behaviour of Normal- and High-Strength Concrete Beams Reinforced with GFRP Bar, Using Different Amounts of Transverse Reinforcement. *Structures* **2021**, *34*, 3113–3124. [[CrossRef](#)]
30. Yousefi Moghadam, S.; Ranjbar, M.M.; Madandoust, R.; Kazemi, M. Analytical Study on the Behavior of Corrosion-Damaged Reinforced Concrete Beams Strengthen with FRP. *Rev. Romana De Mater.* **2017**, *47*, 514–521.
31. Godat, A.; Alghafri, E.; Al Tamimi, N.; Aljaberi, H.; Aldaweela, S. Bond Behavior of Basalt Fiber Reinforced Polymer Bars in Recycled Coarse Aggregate Concrete. *Sustainability* **2022**, *14*, 1374. [[CrossRef](#)]

32. Tang, Y.; Sun, Z.; Wu, G. Compressive Behavior of Sustainable Steel-FRP Composite Bars with Different Slenderness Ratios. *Sustainability* **2019**, *11*, 1118. [[CrossRef](#)]
33. Abraik, E.; Youssef, M.A.; El-Fitiiany, S.F. Seismic Performance of Hybrid Corrosion-Free Self-Centering Concrete Shear Walls. *Sustainability* **2022**, *14*, 712. [[CrossRef](#)]
34. Ju, M.; Park, Y.; Park, C. Cracking Control Comparison in the Specifications of Serviceability in Cracking for FRP Reinforced Concrete Beams. *Compos. Struct.* **2017**, *182*, 674–684. [[CrossRef](#)]
35. Mohammed, A.A.; Manalo, A.C.; Ferdous, W.; Zhuge, Y.; Vijay, P.V.; Alkinani, A.Q.; Fam, A. State-of-the-Art of Prefabricated FRP Composite Jackets for Structural Repair. *Eng. Sci. Technol. Int. J.* **2020**, *23*, 1244–1258. [[CrossRef](#)]
36. Bencardino, F.; Condello, A.; Ombres, L. Numerical and Analytical Modeling of Concrete Beams with Steel, FRP and Hybrid FRP-Steel Reinforcements. *Compos. Struct.* **2016**, *140*, 53–65. [[CrossRef](#)]
37. Luo, Z.; Sinaei, H.; Ibrahim, Z.; Shariati, M.; Jumaat, Z.; Wakil, K.; Pham, B.T.; Mohamad, E.T.; Khorami, M. Computational and Experimental Analysis of Beam to Column Joints Reinforced with CFRP Plates. *Steel Compos. Struct.* **2019**, *30*, 271–280.
38. Zhang, L.; Sun, Y.; Xiong, W. Experimental Study on the Flexural Deflections of Concrete Beam Reinforced with Basalt FRP Bars. *Mater. Struct.* **2015**, *48*, 3279–3293. [[CrossRef](#)]
39. Adam, M.A.; Said, M.; Mahmoud, A.A.; Shanour, A.S. Analytical and Experimental Flexural Behavior of Concrete Beams Reinforced with Glass Fiber Reinforced Polymers Bars. *Constr. Build. Mater.* **2015**, *84*, 354–366. [[CrossRef](#)]
40. Okelo, R.; Yuan, R.L. Bond Strength of Fiber Reinforced Polymer Rebars in Normal Strength Concrete. *J. Compos. Constr.* **2005**, *9*, 203–213. [[CrossRef](#)]
41. Lee, J.-Y.; Kim, T.-Y.; Kim, T.-J.; Yi, C.-K.; Park, J.-S.; You, Y.-C.; Park, Y.-H. Interfacial Bond Strength of Glass Fiber Reinforced Polymer Bars in High-Strength Concrete. *Compos. Part B: Eng.* **2008**, *39*, 258–270. [[CrossRef](#)]
42. Farghaly, A.S.; Benmokrane, B. Shear Behavior of FRP-Reinforced Concrete Deep Beams without Web Reinforcement. *J. Compos. Constr.* **2013**, *17*, 04013015. [[CrossRef](#)]
43. Andermatt, M.F.; Lubell, A.S. Behavior of Concrete Deep Beams Reinforced with Internal Fiber-Reinforced Polymer-Experimental Study. *ACI Struct. J.* **2013**, *110*, 585.
44. Chen, H.; Yi, W.-J.; Ma, Z.J.; Hwang, H.-J. Modeling of Shear Mechanisms and Strength of Concrete Deep Beams Reinforced with FRP Bars. *Compos. Struct.* **2020**, *234*, 111715. [[CrossRef](#)]
45. Mohamed, A.M.; Mahmoud, K.; El-Salakawy, E.F. Behavior of Simply Supported and Continuous Concrete Deep Beams Reinforced with GFRP Bars. *J. Compos. Constr.* **2020**, *24*, 04020032. [[CrossRef](#)]
46. Zinkaah, O.H.; Ashour, A. Load Capacity Predictions of Continuous Concrete Deep Beams Reinforced with GFRP Bars. *Structures* **2019**, *19*, 449–462. [[CrossRef](#)]
47. Thomas, J.; Ramadass, S. Prediction of the Load and Deflection Response of Concrete Deep Beams Reinforced with FRP Bars. *Mech. Adv. Mater. Struct.* **2021**, *28*, 43–66. [[CrossRef](#)]
48. Mohamed, K.; Farghaly, A.S.; Benmokrane, B. Effect of Web Reinforcement in FRP-Reinforced Deep Beams. In Proceedings of the The 7th International Conference on FRP Composites in Civil Engineering, Vancouver, BC, Canada, 20–22 August 2014.
49. Ashour, A.F. Shear Capacity of Reinforced Concrete Deep Beams. *J. Struct. Eng.* **2000**, *126*, 1045–1052. [[CrossRef](#)]
50. Zinkaah, O.H.; Ashour, A.; Sheehan, T. Experimental Tests of Two-Span Continuous Concrete Deep Beams Reinforced with GFRP Bars and Strut-and-Tie Method Evaluation. *Compos. Struct.* **2019**, *216*, 112–126. [[CrossRef](#)]
51. Madandoust, R.; Kazemi, M. Numerical Analysis of Break-off Test Method on Concrete. *Constr. Build. Mater.* **2017**, *151*, 487–493. [[CrossRef](#)]
52. Kazemi, M.; Kafi, M.A.; Hajforoush, M.; Kheyroddin, A. Cyclic Behaviour of Steel Ring Filled with Compressive Plastic or Concrete, Installed in the Concentric Bracing System. *Asian J. Civ. Eng.* **2020**, *21*, 29–39. [[CrossRef](#)]
53. Madandoust, R.; Bazkilyaei, Z.F.Z.; Kazemi, M. Factor Influencing Point Load Tests on Concrete. *Asian J. Civ. Eng.* **2018**, *19*, 937–947. [[CrossRef](#)]
54. Kazemi, M.; Courard, L. Modelling Thermal and Humidity Transfers within Green Roof Systems: Effect of Rubber Crumbs and Volcanic Gravel. *Adv. Build. Energy Res.* **2020**, 1–26. [[CrossRef](#)]
55. Kazemi, M.; Courard, L. Simulation of Humidity and Temperature Distribution in Green Roof with Pozzolana as Drainage Layer: Influence of Outdoor Seasonal Weather Conditions and Internal Ceiling Temperature. *Sci. Technol. Built Environ.* **2021**, *27*, 509–523. [[CrossRef](#)]
56. De Lorenzis, L.; Scialpi, V.; La Tegola, A. Analytical and Experimental Study on Bonded-in CFRP Bars in Glulam Timber. *Compos. Part B Eng.* **2005**, *36*, 279–289. [[CrossRef](#)]
57. Brózda, K.; Selejda, J.; Koteš, P. Analysis of Properties of the FRP Rebar to Concrete Structures. *Appl. Eng. Lett.* **2017**, *2*, 6–10.
58. Hibbitt, D.; Karlsson, B.; Sorensen, P. *ABAQUS/Standard: User's Manual*; Hibbitt, Karlsson & Sorensen: Pawtucket, RI, USA, 2011; Volume 1.
59. Lee, J.; Fenves, G.L. Plastic-Damage Model for Cyclic Loading of Concrete Structures. *J. Eng. Mech.* **1998**, *124*, 892–900. [[CrossRef](#)]
60. Kmiecik, P.; Kamiński, M. Modelling of Reinforced Concrete Structures and Composite Structures with Concrete Strength Degradation Taken into Consideration. *Arch. Civ. Mech. Eng.* **2011**, *11*, 623–636. [[CrossRef](#)]
61. Michal, S.; Andrzej, W. Calibration of the CDP Model Parameters in Abaqus. In Proceedings of the The 2015 World Congress on Advances in Structural Engineering and Mechanics (ASEM15), Incheon, Korea, 25–29 August 2015.
62. Pillai, S.U.; Kirk, D.W. *Reinforced Concrete Design*, 2nd ed.; McGraw-Hill Inc.: New York, NY, USA, 1988.

63. Jahandari, S.; Mohammadi, M.; Rahmani, A.; Abolhasani, M.; Miraki, H.; Mohammadifar, L.; Kazemi, M.; Saberian, M.; Rashidi, M. Mechanical Properties of Recycled Aggregate Concretes Containing Silica Fume and Steel Fibres. *Materials* **2021**, *14*, 7065. [[CrossRef](#)]
64. Yu, Y.; Rashidi, M.; Samali, B.; Mohammadi, M.; Nguyen, T.N.; Zhou, X. Crack Detection of Concrete Structures Using Deep Convolutional Neural Networks Optimized by Enhanced Chicken Swarm Algorithm. *Struct. Health Monit.* **2022**, 1–20. [[CrossRef](#)]
65. Feng, Y.; Mohammadi, M.; Wang, L.; Rashidi, M.; Mehrabi, P. Application of Artificial Intelligence to Evaluate the Fresh Properties of Self-Consolidating Concrete. *Materials* **2021**, *14*, 4885. [[CrossRef](#)]
66. Shahmansouri, A.A.; Yazdani, M.; Hosseini, M.; Bengar, H.A.; Ghatte, H.F. The Prediction Analysis of Compressive Strength and Electrical Resistivity of Environmentally Friendly Concrete Incorporating Natural Zeolite Using Artificial Neural Network. *Constr. Build. Mater.* **2022**, *317*, 125876. [[CrossRef](#)]
67. Bengar, H.A.; Shahmansouri, A.A. Post-Fire Behavior of Unconfined and Steel Tube Confined Rubberized Concrete under Axial Compression. In Proceedings of the Structures; Elsevier: Amsterdam, The Netherlands, 2021; Volume 32, pp. 731–745.
68. Hasan-Ghasemi, A.; Nematzadeh, M.; Fallahnejad, H. Post-Fire Residual Fracture Characteristics and Brittleness of Self-Compacting Concrete Containing Waste PET Flakes: Experimental and Theoretical Investigation. *Eng. Fract. Mech.* **2022**, *261*, 108263. [[CrossRef](#)]
69. Mohammadifar, L.; Miraki, H.; Rahmani, A.; Jahandari, S.; Mehdizadeh, B.; Rasekh, H.; Samadi, P.; Samali, B. Properties of Lime-Cement Concrete Containing Various Amounts of Waste Tire Powder under Different Ground Moisture Conditions. *Polymers* **2022**, *14*, 482. [[CrossRef](#)] [[PubMed](#)]
70. Mehdizadeh, B.; Jahandari, S.; Vessalas, K.; Miraki, H.; Rasekh, H.; Samali, B. Fresh, Mechanical, and Durability Properties of Self-Compacting Mortar Incorporating Alumina Nanoparticles and Rice Husk Ash. *Materials* **2021**, *14*, 6778. [[CrossRef](#)]
71. Memarzadeh, A.; Shahmansouri, A.A.; Nematzadeh, M.; Gholampour, A. A Review on Fire Resistance of Steel-Concrete Composite Slim-Floor Beams. *Steel Compos. Struct. Int. J.* **2021**, *40*, 13–32.
72. Fallah-Valukolaee, S.; Hashemi, S.K.; Nematzadeh, M. Effect of Steel Fiber on Flexural Performance of Bilayer Concrete Beams with Steel and GFRP Rebars: Experiments and Predictions. *Structures* **2022**, *39*, 405–418. [[CrossRef](#)]
73. Hasan-Ghasemi, A.; Nematzadeh, M. Tensile and Compressive Behavior of Self-Compacting Concrete Incorporating PET as Fine Aggregate Substitution after Thermal Exposure: Experiments and Modeling. *Constr. Build. Mater.* **2021**, *289*, 123067. [[CrossRef](#)]
74. Chen, F.; Jin, Z.; Wang, E.; Wang, L.; Jiang, Y.; Guo, P.; Gao, X.; He, X. Relationship Model between Surface Strain of Concrete and Expansion Force of Reinforcement Rust. *Sci. Rep.* **2021**, *11*, 1–11. [[CrossRef](#)]
75. Huang, H.; Huang, M.; Zhang, W.; Yang, S. Experimental Study of Predamaged Columns Strengthened by HPFL and BSP under Combined Load Cases. *Struct. Infrastruct. Eng.* **2021**, *17*, 1210–1227. [[CrossRef](#)]
76. Tan, K.; Qin, Y.; Du, T.; Li, L.; Zhang, L.; Wang, J. Biochar from Waste Biomass as Hygroscopic Filler for Pervious Concrete to Improve Evaporative Cooling Performance. *Constr. Build. Mater.* **2021**, *287*, 123078. [[CrossRef](#)]
77. Shi, T.; Lan, Y.; Hu, Z.; Wang, H.; Xu, J.; Zheng, B. Tensile and Fracture Properties of Silicon Carbide Whisker-Modified Cement-Based Materials. *Int. J. Concr. Struct. Mater.* **2022**, *16*, 1–13. [[CrossRef](#)]
78. Muhammad, N.Z.; Shafaghat, A.; Keyvanfar, A.; Abd. Majid, M.Z.; Ghoshal, S.K.; Mohammadyan Yasouj, S.E.; Ganiyu, A.A.; Samadi Kouchaksaraei, M.; Kamyab, H.; Taheri, M.M.; et al. Tests and Methods of Evaluating the Self-Healing Efficiency of Concrete: A Review. *Constr. Build. Mater.* **2016**, *112*, 1123–1132. [[CrossRef](#)]
79. Talaiekhazani, A.; Keyvanfar, A.; Andalib, R.; Samadi, M.; Shafaghat, A.; Kamyab, H.; Majid, M.Z.A.; Zin, R.M.; Fulazzaky, M.A.; Lee, C.T.; et al. Application of Proteus Mirabilis and Proteus Vulgaris Mixture to Design Self-Healing Concrete. *Desalination Water Treat.* **2014**, *52*, 3623–3630. [[CrossRef](#)]
80. Ponraj, M.; Talaiekhazani, A.; Zin, R.M.; Ismail, M.; Abd Majid, M.Z.; Keyvanfar, A.; Kamyab, H. Bioconcrete Strength, Durability, Permeability, Recycling and Effects on Human Health: A Review. *Int. J. Civ. Struct. Eng. IJCSSE* **2015**, *2*, 118–126.
81. Shariati, M.; Ramli Sulong, N.H.; Arabnejad, M.; Mahoutian, M. Shear Resistance of Channel Shear Connectors in Plain, Reinforced and Lightweight Concrete. *Sci. Res. Essays* **2011**, *6*, 977–983.
82. Luo, Y.; Zheng, H.; Zhang, H.; Liu, Y. Fatigue Reliability Evaluation of Aging Prestressed Concrete Bridge Accounting for Stochastic Traffic Loading and Resistance Degradation. *Adv. Struct. Eng.* **2021**, *24*, 3021–3029. [[CrossRef](#)]
83. Liu, W.; Guo, Z.; Wang, C.; Niu, S. Physico-Mechanical and Microstructure Properties of Cemented Coal Gangue-Fly Ash Backfill: Effects of Curing Temperature. *Constr. Build. Mater.* **2021**, *299*, 124011. [[CrossRef](#)]
84. Dong, H.-L.; Zhou, W.; Wang, Z. Flexural Performance of Concrete Beams Reinforced with FRP Bars Grouted in Corrugated Sleeves. *Compos. Struct.* **2019**, *215*, 49–59. [[CrossRef](#)]
85. Mohtaj Khorasani, A.M.; Esfahani, M.R. Effect of Concrete Strength, Arrangement/Ratio of Reinforcement on Flexural Behavior and Cracking of Concrete Beams Reinforced with GFRP Bars. *J. Struct. Constr. Eng.* **2018**, *7*, 88–107.